Cell

Resource

# The cycling and aging mouse female reproductive tract at single-cell resolution

## Graphical abstract

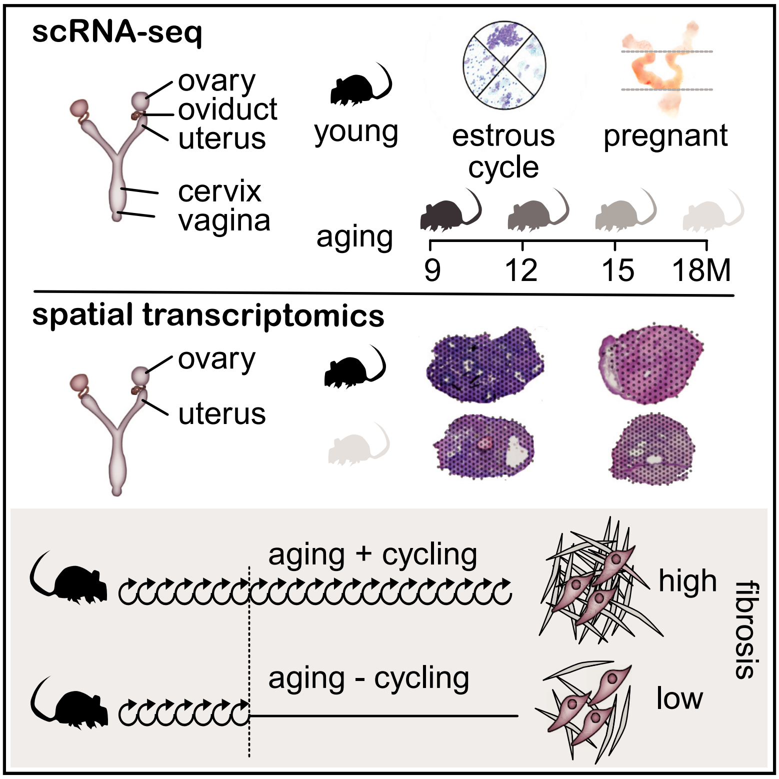

## Highlights

- Spatial and single-cell study of the cycling and aging female reproductive tract
- Inflammation and ECM are recurrently modulated in the cycling female reproductive tract
- Fibroblast control of inflammation and ECM remodeling is highly organ-specific
- Fibrosis results from incomplete resolution of cyclic organ remodeling

## Authors

Ivana Winkler, Alexander Tolkachov, Fritjof Lammers, ..., Simon Haas, Duncan T. Odom, Ângela Gonçalves

## Correspondence

d.odom@dkfz-heidelberg.de (D.T.O.),
a.goncalves@dkfz-heidelberg.de (Â.G.)

## In brief

A spatial and single-cell atlas of the mouse female reproductive tract details transcriptional and cellular abundance changes occurring across estrous cycling, pregnancy, and aging, revealing how cycling-related remodeling contributes to inflammation and fibrotic development.

Winkler et al., 2024, Cell *187*, 981–998
February 15, 2024
https://doi.org/10.1016/j.cell.2024.01.021

CellPress

Cell

CellPress
OPEN ACCESS

Resource

# The cycling and aging mouse female reproductive tract at single-cell resolution

Ivana Winkler,[1,14] Alexander Tolkachov,[2,14,16] Fritjof Lammers,[2,15] Perrine Lacour,[1,3,15] Klaudija Daugelaite,[2,3,15] Nina Schneider,[1] Marie-Luise Koch,[2] Jasper Panten,[2,3,4] Florian Grünschläger,[3,5,6] Tanja Poth,[7] Bianca Machado de Ávila,[8] Augusto Schneider,[8] Simon Haas,[5,6,9,10,11,12] Duncan T. Odom,[2,13,*] and Ângela Gonçalves[1,17,*]

[1]German Cancer Research Center (DKFZ), Division of Somatic Evolution and Early Detection, 69120 Heidelberg, Germany
[2]German Cancer Research Center (DKFZ), Division of Regulatory Genomics and Cancer Evolution, 69120 Heidelberg, Germany
[3]Heidelberg University, Faculty of Biosciences, 69117 Heidelberg, Germany
[4]German Cancer Research Center (DKFZ), Division of Computational Genomics and Systems Genetics, 69120 Heidelberg, Germany
[5]German Cancer Research Center (DKFZ) and DKFZ–ZMBH Alliance, Division of Stem Cells and Cancer, 69120 Heidelberg, Germany
[6]Heidelberg Institute for Stem Cell Technology and Experimental Medicine (HI-STEM gGmbH), 69120 Heidelberg, Germany
[7]CMCP - Center for Model System and Comparative Pathology, Institute of Pathology, University Hospital Heidelberg, 69120 Heidelberg, Germany
[8]Universidade Federal de Pelotas, Faculdade de Nutrição, 96010-610 Pelotas, RS, Brazil
[9]Berlin Institute of Health (BIH) at Charité – Universitätsmedizin Berlin, 10117 Berlin, Germany
[10]Berlin Institute for Medical Systems Biology, Max Delbrück Center for Molecular Medicine in the Helmholtz Association, 10115 Berlin, Germany
[11]German Cancer Consortium (DKTK), 69120 Heidelberg, Germany
[12]Charité - Universitätsmedizin Berlin, Department of Hematology, Oncology and Cancer Immunology, 10115 Berlin, Germany
[13]Cancer Research UK - Cambridge Institute, University of Cambridge, Cambridge, UK
[14]These authors contributed equally
[15]These authors contributed equally
[16]Present address: Department of Cardiology, Angiology and Pneumology, Internal Medicine III, Heidelberg University Hospital, 69120 Heidelberg, Germany
[17]Lead contact
*Correspondence: d.odom@dkfz-heidelberg.de (D.T.O.), a.goncalves@dkfz-heidelberg.de (Â.G.)
https://doi.org/10.1016/j.cell.2024.01.021

## SUMMARY

The female reproductive tract (FRT) undergoes extensive remodeling during reproductive cycling. This recurrent remodeling and how it shapes organ-specific aging remains poorly explored. Using single-cell and spatial transcriptomics, we systematically characterized morphological and gene expression changes occurring in ovary, oviduct, uterus, cervix, and vagina at each phase of the mouse estrous cycle, during decidualization, and into aging. These analyses reveal that fibroblasts play central—and highly organ-specific—roles in FRT remodeling by orchestrating extracellular matrix (ECM) reorganization and inflammation. Our results suggest a model wherein recurrent FRT remodeling over reproductive lifespan drives the gradual, age-related development of fibrosis and chronic inflammation. This hypothesis was directly tested using chemical ablation of cycling, which reduced fibrotic accumulation during aging. Our atlas provides extensive detail into how estrus, pregnancy, and aging shape the organs of the female reproductive tract and reveals the unexpected cost of the recurrent remodeling required for reproduction.

## INTRODUCTION

During the estrous cycle, the mammalian female reproductive tract (FRT) undergoes extensive remodeling in preparation for ovulation and pregnancy. The physiological changes to the FRT are similar between humans and other mammals, with the notable exception of the human-specific spontaneous terminal differentiation of endometrial stromal cells (SCs).[1] These terminally differentiated cells subsequently break down and are shed during menstruation. In most other mammals, this final differentiation requires a fertilized egg and can be modeled by inducing pregnancy.[2] The reproductive cycle's effect on the multiple organs of the FRT remains incompletely characterized. Prior analyses of the mammalian estrous cycle have had a number of limitations: they were often microscopy-based,[3–8] only analyzed individual organs of the FRT,[9–13] only assayed the activity of one or few genes,[14,15] used bulk tissues,[16] and/or have been primarily qualitative.[17]

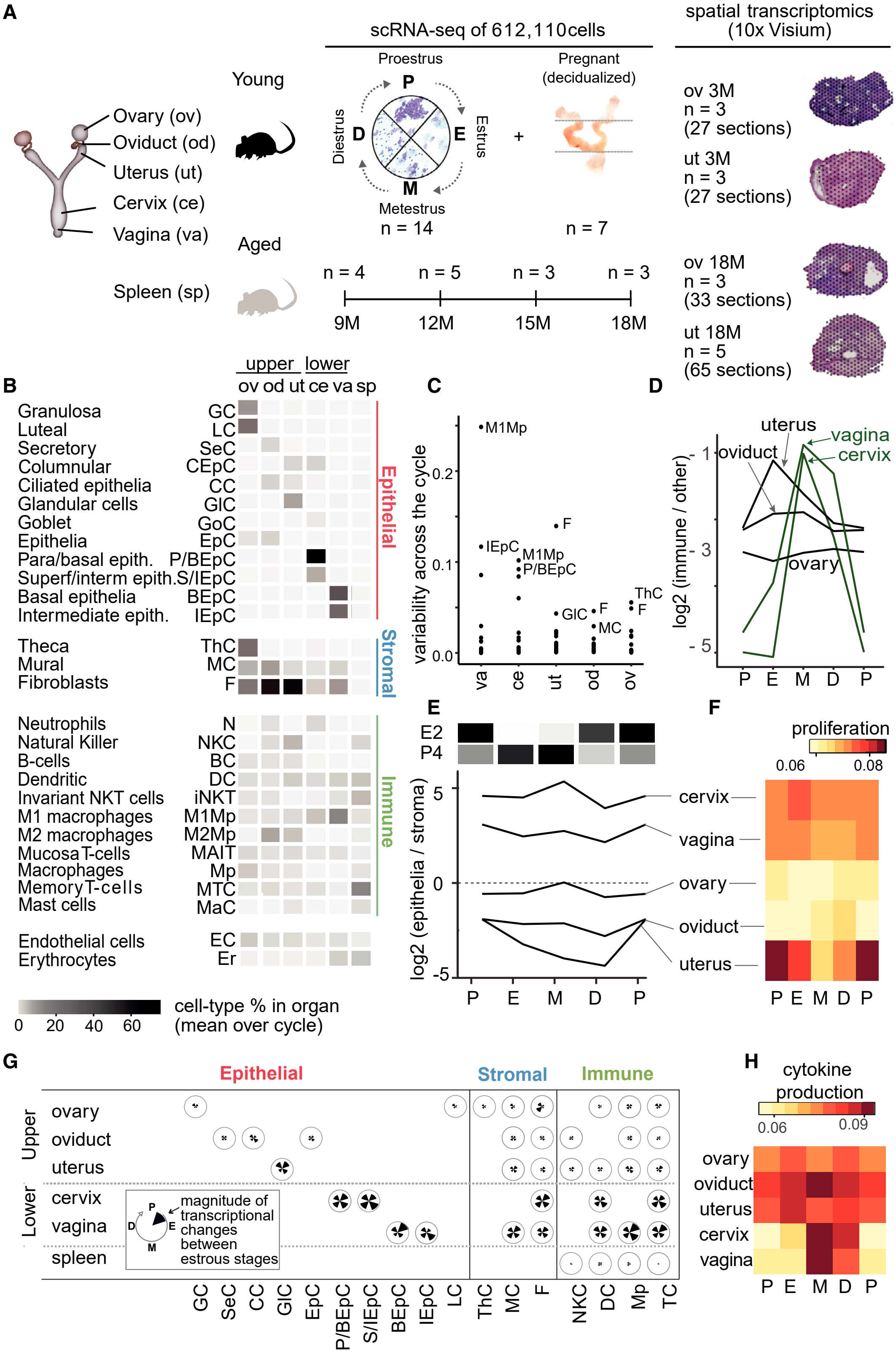

*(legend on next page)*

A remarkable feature of the FRT is its capacity to resolve cyclical inflammatory events rapidly and re-establish normal reproductive function. Unresolved inflammation and remodeling due to aging or other factors can lead to chronic inflammation and fibrosis.[18] In mammals, many conserved reproductive processes display hallmark signs of inflammation[19] and extracellular matrix (ECM) remodeling,[20] both of which are orchestrated by fibroblasts, a key source of inflammatory cytokines and ECM components.[21] Failure of fibroblasts to return to homeostasis can result in persistence of inflammation and ECM production.[21–23]

The FRT organs vary extensively in their susceptibility to age-related pathologies. With aging, the decrease and ultimate exhaustion of ovarian follicles results in diminished estrogen production[24] and the cessation of ovarian cycling. This is accompanied by extensive physiological changes to all FRT organs.[25] Exogenous restoration of estrogen can alleviate some, but not all, age-related physiological changes, as the decrease in pregnancy and implantation rates appear irreversible.[26,27]

To explore how the FRT is remodeled during the female lifetime, we characterized at single-cell resolution ovary, oviduct, uterus, cervix, and vagina at each phase of the mouse estrous cycle, during decidualization, and into old age. Our analyses reveal that the physiological differences between the upper (ovary, oviduct, uterus) and lower reproductive tract (cervix, vagina) are closely mirrored by compositional and transcriptional differences. We discovered that fibroblasts play a key role in shaping the cyclic inflammation and remodeling that naturally occur during the estrous cycle via their cell-cell communication networks. Finally, we provide direct evidence that these recurring cyclic changes contribute to the age-related accumulation of fibrosis and inflammation in the FRT.

## RESULTS

### Single-cell characterization of the cycling FRT

We profiled how the FRT is remodeled during the estrous cycle, decidualization, and aging using single-cell RNA sequencing (scRNA-seq) and spatial transcriptomics. To accurately and robustly quantify the compositional and transcriptional dynamics of the FRT, every experiment in each condition was mapped by between three and seven biological replicates. We characterized the cellular composition and transcriptional states present in FRT organs, and spleen as a control organ, by collecting 378,516 single-cell transcriptomes from normally cycling young mice in each of the four cycle phases (proestrus [P], estrus [E], metestrus [M], and diestrus [D]), as well as 30,966 cells from early pregnancy, 128,499 cells from an aging time course, and 74,129 cells from acyclic old mice (Figure 1A; Table S1). Additionally, to explore *in vivo* spatial transcriptional landscapes, we used the 10× Visium system to profile 27 sections of young ovaries in D, 33 sections of acyclic old ovaries, 27 sections of young uteruses in D, and 65 sections of old uteruses in three to five biological replicates (Figure 1A).

In young cycling mice, we analyzed the single-cell transcriptomes from all cycle phases and organs to identify cell types and their organ specificity. We annotated cell types by combining two automated approaches with extensive manual comparison of marker gene expression (STAR Methods). We identified approximately 50 cell types, including all expected stromal, epithelial, and immune-cell sub-populations (Figures 1B, S1A, and S1B; Table S2).

We identified cell types shared across the entire FRT and quantified the shift in cell-type compositions between the upper and lower tracts (Figure 1B). The composition of the immune compartment profoundly shifts between the upper and lower tracts; the upper tract is enriched in adaptive immune cells, whereas the lower reproductive tract is dominated by innate immune cells (Figure S1C). In addition, the balance between M1 and M2 macrophages profoundly changes between organs (Figure S1D). In the uterus and oviduct, wound-healing-associated M2 macrophages dominate the cellular landscape, where they are likely involved in hormonally induced tissue remodeling.[29] In contrast, the pro-inflammatory M1 macrophages dominate the ovary, where they are required for folliculogenesis.[30] M1 macrophages are also prevalent in cervix and vagina, consistent with their higher pathogen exposure. Similar to human, mouse natural killer cells are concentrated in the uterus.[31]

Our comprehensive analyses of all five FRT organs identified their component cell types, quantified the compositional

**Figure 1. The estrous cycle drives organ-specific compositional changes**

(A) Single-cell analysis was performed on the ovary, oviduct, uterus, cervix, and vagina, with the spleen as a nonreproductive control organ. All organs were profiled in multiple biological replicates at the four phases of the estrous cycle, during aging, and pregnancy. Vaginal smears were used to stage mice in proestrus (P), estrus (E), metestrus (M), and diestrus (D). See also Figure S1E. Spatial transcriptomics was performed on multiple sections of young and old ovaries and uteruses in three biological replicates.

(B) Proportional heatmap of the most abundant cell types by organ.

(C) The compositional variability across the cycle for each cell type in each organ, shown as an interquartile range. The two most variable cell types per organ are indicated. Uncertainty estimates are shown in Figure S2B.

(D) The ratio of immune to other cells across the cycle. The ratios shown are the average across biological replicates, standard errors are shown in Figure S2C. The second P point is a repetition of the first P point to allow easier comparison between diestrus and proestrus.

(E) The ratio of epithelia to stroma across the cycle. The relative concentration of estradiol (E2) and progesterone (P4) at each stage[28] is shown above (black is the maximum value of the cycle, white is 0).

(F) Average activity score of genes promoting cell proliferation (GO:0008284) in epithelial cells. See also Figure S3A. p values indicating significance of pathway activity scores between estrous cycle phase are listed in Table S7.

(G) Similarity of gene expression between the cycle phases for each cell type, quantified using optimal transport and displayed as a flower plot (inset). Petal lengths indicate magnitude of transcriptional changes; for example, most cell types are more transcriptionally dynamic in the cervix and vagina than in the upper FRT.

(H) Average activity score of cytokine regulatory genes (GO:0001816) in immune cells. p values indicating significance of pathway activity scores between estrous cycle phase are listed in Table S7.

differences between organs, and revealed an anti- versus pro-inflammatory transition between the upper and the lower tract.

## Estrous cycling dramatically remodels the cervical and vaginal immune compartments

To understand how tissue environment, hormone state, and intrinsic cell identity combine to shape each organ's tissue landscape, we assessed how the cellular composition of the FRT varies across the estrous cycle. We precisely staged the cycle phase of each mouse by identifying the cell types present in vaginal smears (Figure S1E; STAR Methods), which we confirmed by unbiased reconstruction of the transcriptional pseudotime trajectory of uterine stromal fibroblasts (Figure S1F; STAR Methods). Indeed, the cells identified in smears (Figure S1E) were consistent with vaginal single-cell data. For example, the proportion of nucleated epithelial cells (such as basal epithelial cells [BEpC] and intermediate epithelial cells [IEpcC]) is highest in P and lowest at M (Figures S1G and S2A).

We quantified which cell types are most variable in each organ by calculating the inter-quartile range of cell-type proportions across the cycle (STAR Methods). The vagina has the most cycle-variable cell types as well as the highest average amplitude of compositional changes in the FRT (Figures 1C and S2B). In the uterus and cervix, fewer cell types vary across the cycle, while the oviduct and ovary are relatively invariant in their composition.

We then asked how the immune compartment of the FRT is remodeled across the cycle (Figures 1D, S2A, S2C, and S2D). We found that the fraction of immune cells is lowest during P and E in the lower FRT organs. The vagina and cervix show considerably greater variation in their content of immune cells, with a maximum at M, while the ovary and oviduct remain relatively invariant. For the vagina, we independently confirmed the sharp increase in immune cell numbers in M by quantifying the fraction of immune cells across the cycle via flow cytometry (Figures S1H and S2E). In the uterus, the immune cell proportion is modestly modulated across the cycle. Although there is considerable variability across biological replicates, immune-cell proportion seems to peak earlier at E, followed by a slower decline. This observation suggests a mechanism for the enhanced bacterial surveillance specific to E phase previously observed.[32]

For specific immune cell types, we saw shifts in cell sub-population abundances during estrous cycling. For instance, in oviduct M1 macrophage abundance peaks at E, whereas M2 abundance peaks at M (Figures S2A and S2D). In the uterus, both M1 and M2 abundances peak during E, whereas natural killer (NK) abundance is highest at M.

Our analyses newly quantified how the different organs of the FRT are immunologically distinct. The lower reproductive tract undergoes cyclical, acute immune influx, which is also seen to a smaller extent in the uterus, while the ovary and oviduct maintain a relatively invariant population of immune cells. More generally, the variation in immune cell composition and activation could explain why immune responses and protection of the reproductive system (e.g., vaccine-induced immunity) have been previously reported to vary along the cycle.[33]

The cycle dynamics of cellular abundance can be explored in an interactive online tool (see Data and code availability).

## Uterus undergoes profound cyclical epithelial to stromal remodeling

Cell proliferation and death can be regulated by systemic steroid hormones.[34] To evaluate whether tissue proliferation and remodeling is synchronized among the five organs of the FRT, we calculated the ratio of epithelia to stroma (Figures 1E and S2F). With the exception of the uterus, FRT organs are relatively stable throughout the cycle. In the uterus, the ratio of epithelial to stromal peaks in P, likely due to an increase in epithelial proliferation coincident with the estrogen (E2) surge (P versus M, linear mixed model, padj = 0.028) (Figures 1E, 1F, and S3A; Table S7). In contrast, progesterone promotes stromal proliferation and inhibits E2-induced epithelial proliferation,[35] and, indeed, stromal proliferation coincides with peak progesterone levels and is greatest at E and M (Figures S2G and S3B).

The most notable contrast in tissue remodeling is between the vagina and uterus. In the vagina, there are cell-type-specific changes within the epithelial compartment across the cycle (Figures 1C and S1G) that do not impact the overall balance of epithelia to stroma (Figure 1E). In contrast, the uterus shows strong changes in its epithelial to stromal ratio (Figure 1E).

In sum, our data reveal how epithelial/stromal proliferation is precisely regulated during the cycle. The regulation of cell-type abundances in the FRT is highly organ-specific, despite the influence of systemic sex hormones.

## Tissue morphological changes are tracked by gene expression

We considered the possibility that organs such as the ovary and oviduct, where cell abundances are relatively stable across the cycle, might instead show substantial changes in transcription. We scored the magnitude of transcriptional change between phases of the cycle for each cell type in every FRT organ using optimal transport analysis (STAR Methods; Figure 1G). This analysis revealed that the vagina and cervix are high in both cell-type variability and gene expression changes; in contrast, the cells in the uterus, oviduct, and ovary show less of both (Figures 1C and 1G). Similarly, the abundance of immune cells closely corresponds to their functional activation, which we orthogonally measured by single-cell scoring of cytokine gene expression (Figures 1H and S3C; Table S7).

Thus, organs with the largest morphological changes also have the largest transcriptional changes across all cell types.

## Fibroblast functions are dynamically regulated throughout the cycle, but not coordinated between organs

In nonreproductive tissues, fibroblasts control inflammation and wound healing.[36] We considered whether fibroblasts may play the same functional roles in the different cycling FRT organs. We first used over-representation analysis to identify the functional pathways enriched among genes with significant differential expression between adjacent cycle phases (Figure 2A; STAR Methods). This revealed that ECM remodeling and tumor necrosis factor (Tnf) regulation of inflammation are core programs of fibroblasts during the cycle. However, between organs, the activity of these two functional pathways assessed using AUCell

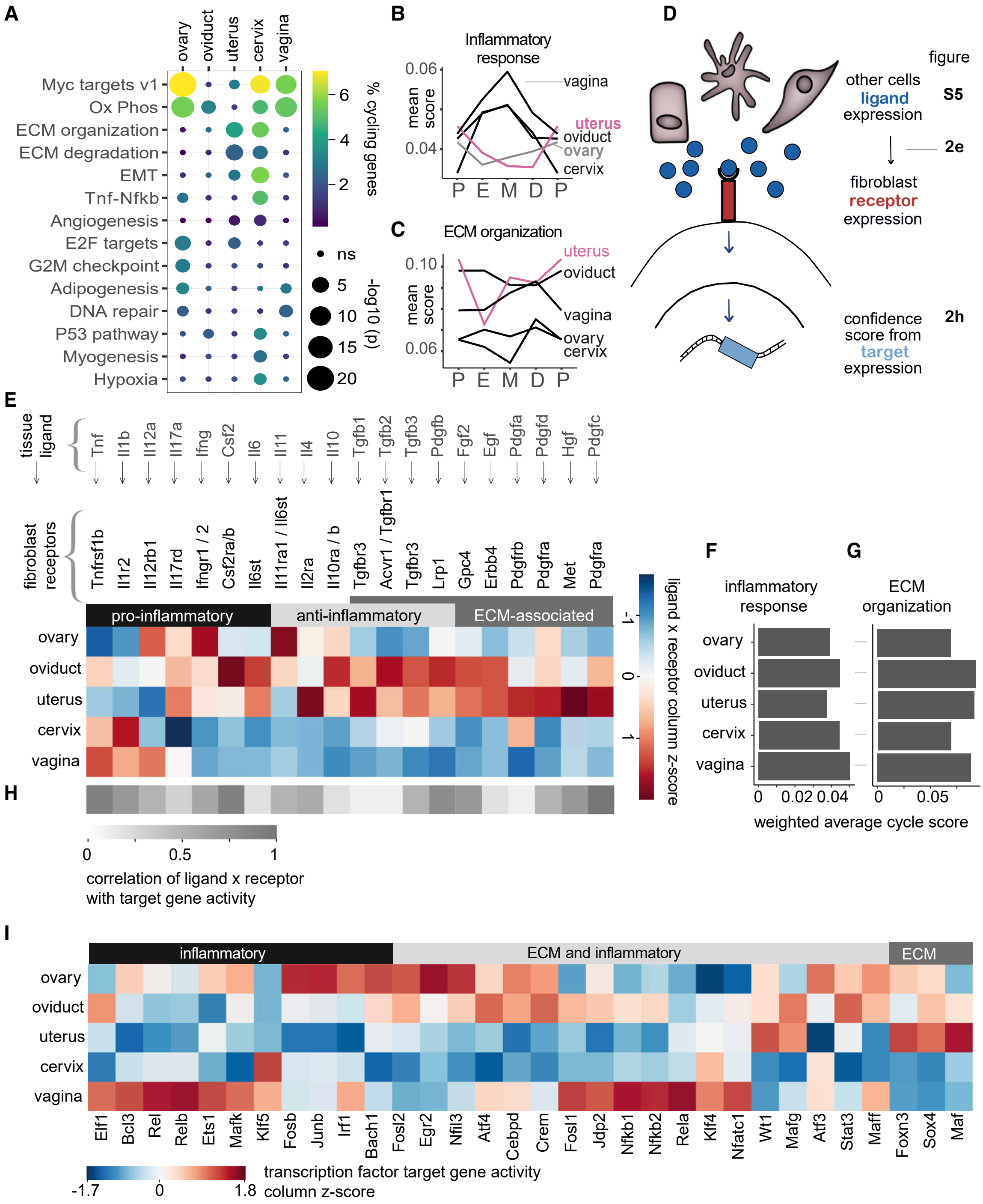

**Figure 2. Gene expression dynamics of fibroblasts across the FRT**

(A) Functional pathways enriched in genes differentially expressed between phases of the cycle in fibroblasts.

(B) Activity scores of inflammatory genes averaged across all fibroblasts in each phase. See also Figure S3D. p values indicating significance of pathway activity scores between estrous cycle phase are listed in Table S7.

(C) Activity scores of ECM organization genes, as in (B). See also Figure S3E. p values indicating significance of pathway activity scores between estrous cycle phase are listed in Table S7.

(D) Schematic of the cell-to-cell ligand-receptor and ligand-target analyses.

(E) *Z* scores of ligand-receptor products averaged across phases. Ligand expression is averaged across all cell types; receptors are in fibroblasts only. See also Figure S4A. The receptor-ligand interactions shown were deemed significantly different between FRT organs by a permutation test (Table S4).

(legend continued on next page)

is often out of phase or even anti-correlated (Figures 2B, 2C, S3D, and S3E; Table S7; STAR Methods).

The activation of inflammatory pathways in fibroblasts shows two organ-specific patterns (Figure 2B): in the vagina, cervix, and oviduct, inflammation peaks at M, and in the uterus and ovary, it peaks at P. Thus, the vaginal immune cell infiltration we previously observed at M (Figure S1G) is accompanied by fibroblast inflammatory activation. In contrast, ECM organization shows no coordinated pattern across FRT organs (Figure 2C). Compared with the other organs, the uterus has the most extensive ECM remodeling, which peaks at P and reaches its minimum during E (padj = 0.08, P versus E, linear mixed model).

We considered whether FRT organs from the same mouse shared a similar inflammatory state. This is not the case: differences in inflammation activity scores are primarily tissue specific and not individual specific (Figure S3F).

Our data show that cycling fibroblast programs are similar between organs, yet often out of phase, suggesting that fibroblast functions are regulated by a combination of systemic and local cues. Differentially and co-expressed gene clusters can be explored in our interactive online tool (Data and code availability).

## Cell-cell communication and transcription factor activity reveal high inflammation in the lower FRT and extensive ECM remodeling in the uterus

Fibroblasts coordinate organ function and homeostasis via communication with other cell types through ligand-receptor interactions.[21,37] We performed cell-to-cell communication analysis to identify the activity of ligand-receptor interactions and their organ specificity (Figure 2D; STAR Methods). We focused on how ligands from all cell types converged on fibroblasts by calculating communication scores as the product between (1) the expression of ligands averaged over all cell types in all phases (the "ambient" ligand expression) and (2) the expression of receptors averaged over fibroblasts in all phases (Figures 2E and S4A; Table S4; STAR Methods).

Vaginal and cervical fibroblasts have the highest communication scores for pro-inflammatory Tnf and Il1b and the lowest scores for anti-inflammatory Il10, Il11, and Tgfb (Figures 2E and S4A). In contrast, uterine fibroblasts receive primarily anti-inflammatory signaling and the oviduct and ovary have a mixture of anti- and pro-inflammatory signaling. For each organ, we averaged the inflammation scores across the cycle and found that the vagina has the strongest responses (Figure 2F). A similar analysis of ECM reorganization demonstrated that the uterus and oviduct undergo the largest structural remodeling, followed by the vagina (Figure 2G). Indeed, fibroblasts in the uterus and oviduct show the highest communication scores for ECM-associated signaling (Figures 2E and S4A). Most notably, these tissues show the highest activity of transforming growth factor b (TGFb) signaling, which is considered to be the master regulator of fibrosis.[38] We verified that increased cell-to-cell communication activates downstream pathways in fibroblasts for most of the ligands by scoring the activity of their target genes[39] (Figures 2H and S4B; STAR Methods). Thus, if an organ has high ligand-receptor activity, then it has high ligand-target activity.

Finally, to identify candidate regulators involved in organ-specific inflammatory and ECM processes, we quantified the associated transcription factor activity across the cycle using Single-cell regulatory network inference and clustering (SCENIC) (Figure 2I; STAR Methods). As expected, we found that the activity of inflammation-associated transcription factors is highest in the vagina, while the activity of ECM-related transcription factors is highest in the uterus (Figure 2I).

We confirmed that fibroblasts are central regulators of inflammation and ECM across the FRT. We discovered that the timing and underlying transcriptional regulators of fibroblast activation are highly organ-specific. Cell-to-cell communication and transcription factor activity can be explored in our interactive online tool (Data and code availability).

## Signaling to fibroblasts is highly organ-specific

We then sought to identify which cell types were responsible for signaling to fibroblasts by partitioning the transcription of each ligand by cell-of-origin (Figure S5; STAR Methods). In the lower reproductive tract, M1 macrophages (source of *Il1b*, *Tnf*, *Il12a*) and memory T cells (source of *Ifng*, *Csf2*) appear to be responsible for most pro-inflammatory signaling. In the upper reproductive tract, M2 macrophages (source of *Il10*) and fibroblasts/theca cells (source of *Il11*) generate the predominantly anti-inflammatory environment (Figure S5). Our findings agree with studies in other organ systems, which have identified macrophages as primary producers of *Tnf* and *Il12a* and T cells as producers of *Ifng*.[40] The cell types responsible for inflammatory ligand production are often organ-specific; in contrast, fibroblast ECM is generally autocrine-controlled by signaling from SCs (Figure S5).

We also evaluated the estrous cycle dynamics of inflammation-associated cell-to-cell communication in the vagina and uterus. In the vagina, M shows a combination of high pro-inflammatory and low anti-inflammatory ligand-receptor activity (Figure S4C). The main source of pro-inflammatory ligands are T cells (*Csf2*) and macrophages (*Il1b*), which infiltrate the tissue at this phase (Figures S1G, S2A, and S5). The main source of anti-inflammatory signaling are epithelial cells (*Tgfb*) (Figure S5), which proportionally decrease at this phase (Figures S1G and S2A). In the uterus, at M and D, we observe an increase in anti-inflammatory ligand signaling (e.g., Tgfb) (Figure S4D) due to expansion of SCs (Figure 1E), which are the main source of *Tgfb* ligands (Figure S5). At the same time, we observed a decrease in anti-inflammatory ligand signaling (e.g., Tnf) (Figure S4D), which is caused by the decrease in the immune cell proportion (Figures 1D and S5).

---

(F) Activity scores of inflammatory genes averaged across all fibroblasts in each phase in each organ. These scores are the average of the scores shown in (B), weighted by phase length.

(G) Activity scores of ECM genes, as in (F). These scores are the average of the scores shown in (C), weighted by phase length.

(H) Spearman correlation across organs between the expression product of a ligand-receptor pair and the activity score of predicted targets of the ligand.

(I) Averaged activity scores of targets of transcription factors associated with inflammation and ECM regulation in fibroblasts. Shown activity scores were significantly different between the FRT organs by a permutation test (STAR Methods).

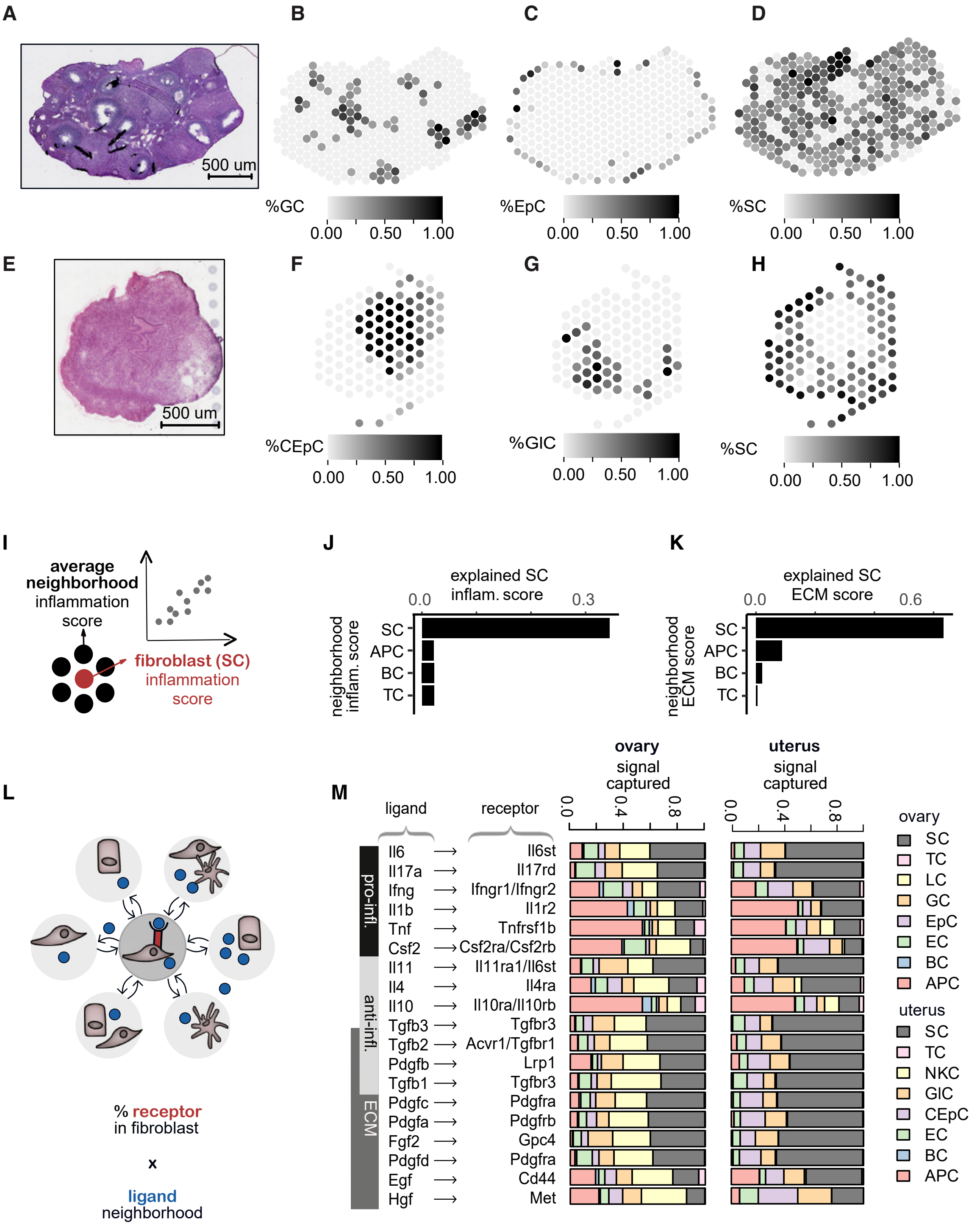

**Figure 3. Spatial niches of fibroblasts with high inflammatory and ECM remodeling activity**

(A) H&E staining of the young ovary. Scale bars, 500 μm.

(B–D) Proportion of granulosa (GC) (B), epithelial (EpC) (C), and stromal cells (SC) (D) per spot in the ovary shown in (A).

(E) H&E staining of the young uterus.

(F–H) Proportion of columnar epithelial (CEpC) (F), glandular (GlC) (G), and stromal cells (SC) (H) per spot in the uterus shown in (E).

(I) Schematics of mixed linear model used to determine the best predictor of fibroblast inflammation score (STAR Methods).

(J) Proportion of SC inflammation scores in the ovary explained by inflammation scores of cell types in the neighborhood.

*(legend continued on next page)*

### Spatial transcriptomics analysis reveals that inflammatory fibroblasts, but not immune cells, shape inflammatory niches

To characterize which cell types shape the microenvironment of fibroblasts, we expanded our analysis with spatially resolved transcriptomics of young ovaries and uteruses. First, we used our droplet-based, single-cell transcriptomes to deconvolute the spatial data into component gene expression profiles of every cell type inside every spot (Figures S6A–S6I; STAR Methods). Our analysis accurately identified specific ovarian structures, including follicles, surface epithelia, and the stroma (Figures 3A–3D). In the uterus, deconvolution similarly revealed the location of the luminal epithelia, glandular epithelia, and the stroma (Figures 3E–3H). The rankings of cell-type proportions in our spatial data and our single-cell data are comparable in both organs, with an under-representation of epithelial cells in single-cell data (Figures S6J and S6K). Next, we used linear mixed models to identify the best predictor of fibroblast inflammation status (Figure 3I; STAR Methods). In both ovary and uterus, fibroblast inflammation is best predicted by inflammation of neighboring SCs (Figures 3J, S6L, and S6M) and poorly predicted by either the activation or proportion of surrounding immune cells (Figures S6L and S6M). Similarly, fibroblast ECM remodeling is best predicted by the ECM activity of surrounding fibroblasts (Figures 3K, S6N, and S6O). Thus, fibroblast autocrine signaling maintains both inflammation and ECM status.

### Fibroblasts are primary consumer cells of most inflammatory and ECM cytokines

Having previously identified the likely ligand-producing cell types, we then sought to identify the likely recipient cell types. To do so, we calculated what fraction of inflammatory and ECM cytokines could potentially be absorbed by each cell type, reflecting their competition as signal sinks[41] (Figure 3L; STAR Methods). This analysis revealed that in both the uterus and the ovary, fibroblasts are the first- or second-best primary consumer cell of most inflammatory and ECM-related cytokines (Figure 3M).

We then more generally leveraged the spatial data to refine our cell-to-cell analysis by explicitly modeling the physical proximity between cell types as well as weighing the communication scores by the fraction of ligand-consuming cell types. We calculated communication scores by multiplying the expression of ligands (averaged over all cell types in the neighborhood) by the expression of receptors (averaged over fibroblasts as in scRNA-seq analysis). This score was weighted by the proportion of signal received by fibroblasts (STAR Methods). The cell-to-cell networks derived from spatial and scRNA-seq based analyses are in good overall agreement (Figures S6P–S6S).

### Modeling the human menstrual cycle using mouse decidualization

During the first trimester of human pregnancy, the immune microenvironment of the decidua prevents inflammatory responses.[42] Here, we first asked whether mouse decidual cells also display an anti-inflammatory profile, and then sought to quantify the degree of transcriptional conservation between human and mouse cycling fibroblasts.

To parallel the spontaneous decidual reaction that occurs during the human cycle, we induced decidualization in mice by inducing pregnancy, and characterized the uterine architecture at embryonic day 5.5 by scRNA-seq in seven biological replicates (Figure 4A). A subset of SCs unique to pregnant mice transcriptionally expresses the classical markers of decidualization: *Alpl*, *Bmp2*, and *Prl8a2* (Figure 4B; see online resource in Data and code availability).[43–45] As expected, many SCs from pregnant uteruses do not express these markers because the mouse uterus decidualizes heterogeneously.[46] We confirmed decidualization histologically using H&E staining (Figure 4C). Compared with the M phase, the pregnant uterus is characterized by the appearance of decidual cells, accompanied by a proportional increase in NK cells, glandular cells (GlCs), and fibroblasts (Figures 4D and S7A). Additionally, to cell compositional changes, decidualization in mice causes extensive transcriptional changes in inflammation, ECM, and embryo development pathways (Figure S7B).

We asked whether the decidualized cells and fibroblasts in mice express the same transcriptional programs previously identified in human uterine fibroblasts (Figures 4E and S7C; Table S5).[13] We used the same mutual information approach as the original study to re-identify 1,670 human genes that are differentially expressed across the menstrual cycle and to identify differentially regulated genes across the mouse estrous cycle (STAR Methods). At every phase of the cycle, the dynamic gene expression changes in human and mouse are more similar than expected by chance (STAR Methods), and the phase of decidualization has an especially high percentage of similarity (Figure 4E). These genes are enriched for ECM, inflammation, and cycle regulation and implantation pathways (Figure S7D). Most of these processes show species-specific differences in activity across the cycle (Figures 4F–4H and S7E); however, the transition to decidualization is largely conserved. When compared with fibroblasts, decidual SCs show consistently lower activity of ECM- and inflammation-related genes (Figures 4G and 4H) and transcription factors (Figure 4I).

In sum, our analyses revealed that mouse decidual cells display a markedly anti-inflammatory transcriptional profile and that the transition to decidualization is largely conserved between mouse and human.

### Aging leads to primordial follicle depletion and immune cell infiltration

We sought to better understand the dynamic age-related changes within the FRT that culminate in acyclicity.[47] We collected longitudinal samples of all five FRT organs to generate tissue pathology and single-cell transcriptomes as well as the spatially resolved transcriptomes of the acyclic 18-month-old ovary and uterus.

(K) Proportion of SC ECM scores in the ovary explained by ECM scores of cell types in the neighborhood.
(L) Schematic of the cell-to-cell ligand-receptor analysis based on spatial data.
(M) Proportion of ligand signal captured by different cell types in the ovary and uterus.
See also Figure S6.

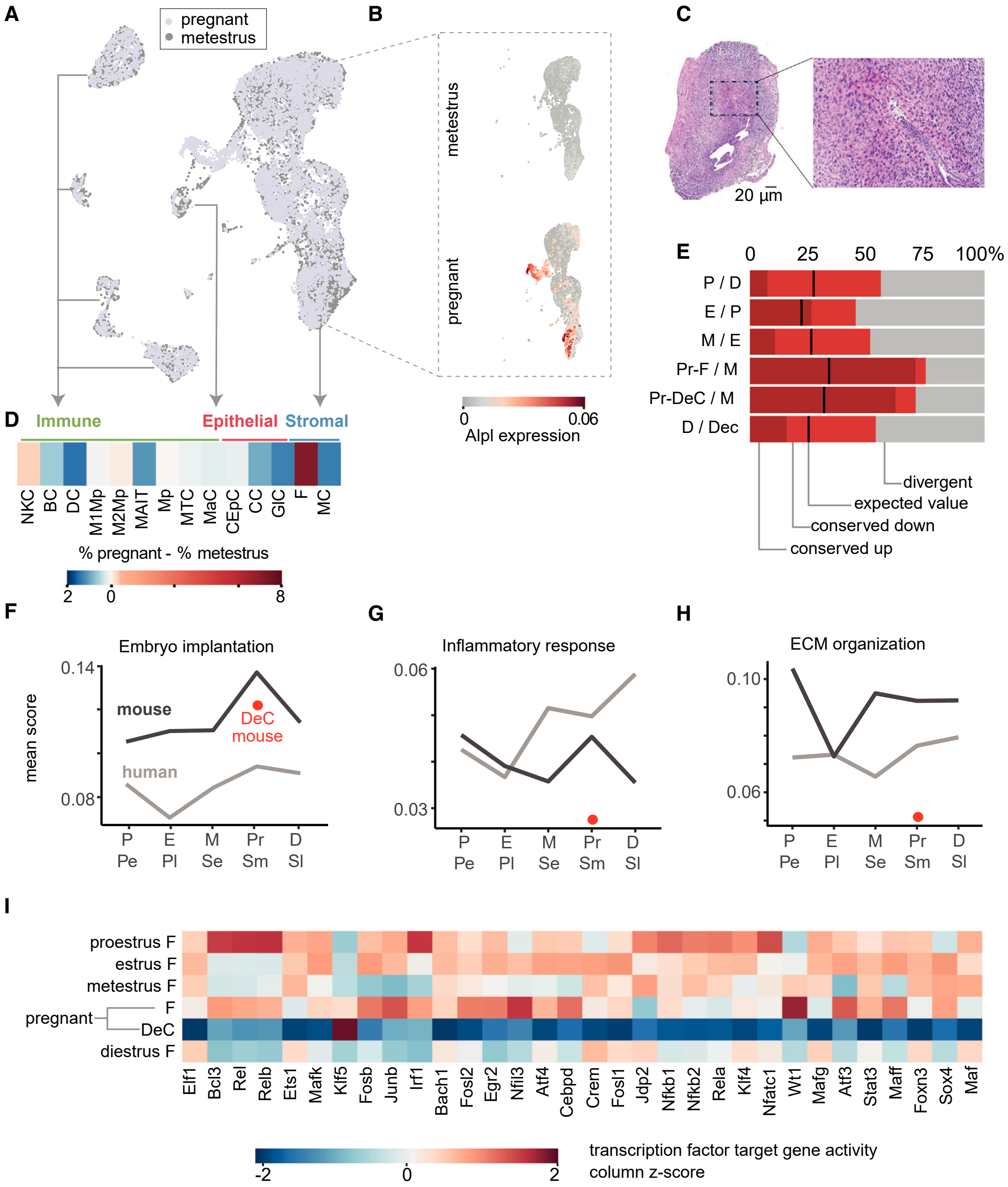

**Figure 4. Regulation of the reproductive cycle and decidualization in mouse and human**

(A) Uniform Manifold Approximation and Projection (UMAP) plot of the integration of the pregnant and metestrus samples. Shown in this panel is a subsample of 19,724 of the total 40,828 cells used in the analyses.

(B) UMAP from (A) subsetted to stromal cells and split by condition showing the expression of marker gene of decidualization *Alpl*.

(C) H&E staining of pregnant mouse uterus showing decidualization at the implantation site. Scale bars, 20 μm.

(D) Difference in average % of each cell type between pregnant and metestrus samples. To compare the changes in other cell types upon decidualization, decidual cells, present only in pregnancy, were omitted and cell abundance was re-calculated.

(E) Differentially expressed genes (DEGs) in mouse uterine fibroblasts and decidual cells and human fibroblasts across the cycles. In red the % of homologous DEGs that showed the same directionality of regulation in paired mouse-human phases (e.g., up-regulation in both species). In gray % of genes that showed opposite directionality of regulation (e.g., up-regulation in humans, down-regulation in mice). Black line shows the % of the conserved genes expected by chance in each phase. As bar labels only mouse phase comparisons are shown (Pr, pregnant; F, fibroblast; DeCs, stromal decidual cells).

*(legend continued on next page)*

Pathology confirmed that 18-month-old mice often display immune infiltration in most organs, atrophy of the ovary, and localized hyperplasias in the ovary and uterus (Figure 5A; see Data and code availability).[48,49] All 18-month-old mice were acyclic, which was uniformly associated with depletion of primordial follicle pools (Figure 5B), similar to the physiology of aged primates and humans.[50,51]

Using our single-cell transcriptomics data, we identified extensive statistically significant changes in cell-type abundances by comparing cell-type proportions between aged and young mice in D (Figures 5C and S8A–S8C), the phase most similar to acyclicity.[49] The ovary shows a decrease in the proportion of follicle-associated cells, such as theca cells (ThC), granulosa cells (GC), and luteal cells (LC), as expected due to the exhaustion of ovarian follicles and corpora lutea in acyclic mice.[52] We independently confirmed this decrease by both histopathology and RNAscope (Figures 5A and S8C). As expected, we found that the proportion of fibroblasts increases in ovary[52] and decreases in the oviduct and uterus.[53]

By evaluating the entire FRT, we quantified how aging increases the fraction of immune cells in the upper reproductive tract, whereas aging decreases the immune cells in the lower reproductive tract. Prior studies on single organs found similar results in isolation.[54–56] The remodeling of the immune compartment is organ-specific: the uterus shows an increase in M1 and M2 macrophages, the cervix and vagina have a decrease in M1 macrophages, while the oviduct has an increase in NK, B, and dendritic cells. The control organ, the spleen, displays statistically significant differences only in invariant NKT cell (iNKT) and plasma cell (PC) proportions (Figures 5C and S8A; Table S3), in agreement with previous reports.[57]

In sum, aging results in substantial changes to the cell-type composition of FRT organs, most notably immune infiltration in the upper reproductive tract.

## Age-related gene expression changes are organ-specific

We then compared the gene expression programs between young and old mice using optimal transport analysis. In contrast with the transcriptional changes associated with the estrous cycle, which are concentrated in the lower FRT, during aging both the upper and lower FRT show extensive gene expression changes (Figure 5D). We found that the magnitude of age-related changes in cell-type transcription is highly organ-specific. For example, fibroblasts show transcriptional changes during aging in all organs, but in the ovary, fibroblasts are the most strongly altered cell type.

In addition to average gene expression changes, an increase in cell-to-cell transcriptional variability has also been shown to be associated with aging,[58,59] though this variability may be cell-type specific.[57] Simultaneously profiling all five FRT organs allowed us to investigate how gene-wise transcriptional variability changes during aging for over 50 different cell types and whether cell types that are common between organs age in a similar manner (Figures 5E, S8D, and S8E; Table S6). We scored the age-associated transcriptional variability against the natural cyclical variation found in these organs using Shannon entropy (STAR Methods; Figure S8E).

Whether FRT organs age at the same rate has been a longstanding debate.[60] Our results indicate that aging strongly increases the cell-to-cell variability in the majority of cell types—especially in the ovary. This age-related phenotype is often cell-type specific: transcriptional variability in mucosa associated T-cells (MAIT) and epithelial cells (EpC) increases substantially with age, whereas in M1 and M2 macrophages it remains largely unaffected (Figures 5E and S8D). Fibroblasts show modest cell-to-cell variability between young and old mice. The transcriptional variability of many epithelial cells (BEpC, columnar epithelial cells [CEpC], and IEpC) is substantially changed with age in the uterus, cervix, and vagina, but by less than the variation observed during normal cycling (Figure S8D).

In sum, the age-related gene expression changes for each cell type are organ-specific, and the age-related increase in cell-to-cell variability is most pronounced in the ovary.

## Organ-specific impact of fibroblast chronic inflammation during FRT aging

Fibroblasts can retain inflammatory memory[22] and thus shape age-related changes to organ physiology and function. To test the extent and impact of inflammatory responses in aged fibroblasts, we measured fibroblast inflammation in the upper FRT of 3-, 9-, 12-, and 15-month-old mice in D, as well as that of 18-month-old acyclic mice, and in the lower FRT of 3-month-old mice in D and of 18-month-old acyclic mice using AUCell (STAR Methods). We then modeled the association of inflammation with age using a linear mixed model (Figure 6A). Aging results in a significant increase in fibroblast inflammation in all organs except the ovary. Interestingly, the rate of increase is significantly different between FRT organs ($p$ value $< 0.05$ of the organ-age interaction terms; STAR Methods), with the cervix and uterus displaying the most pronounced increases.

We quantified what fraction of this inflammation is due to a subset of highly active fibroblasts versus a general increase in all fibroblasts. The distribution of inflammation scores of fibroblasts differed significantly between young and old uteruses (Figure 6B; $p$ value = 0.002, using the waddR package v.1.14.0[61]). We dissected these distributions via decompositional analysis, revealing that they differ in shape, location, and size. In other words, the total increase in fibroblast inflammation is driven by both an expansion of inflamed sub-populations as well as a general increase in inflammation across all fibroblasts.

---

(F) Activity scores of genes that regulate embryo implantation (GO:0007566), averaged across all mouse or human fibroblasts in each phase (Pe, proliferative early; Pl, proliferative late; Se, secretory early; Sm, secretory mid; Sl, secretory late). Red dot indicates the activity score in mouse decidual cells.
(G) Activity scores of inflammatory genes as in (F).
(H) Activity scores of ECM genes as in (F).
(I) Averaged activity scores of targets of transcription factors associated with inflammation and ECM in mouse fibroblasts and decidual cells, across the cycle and in pregnancy.
See also Figure S7.

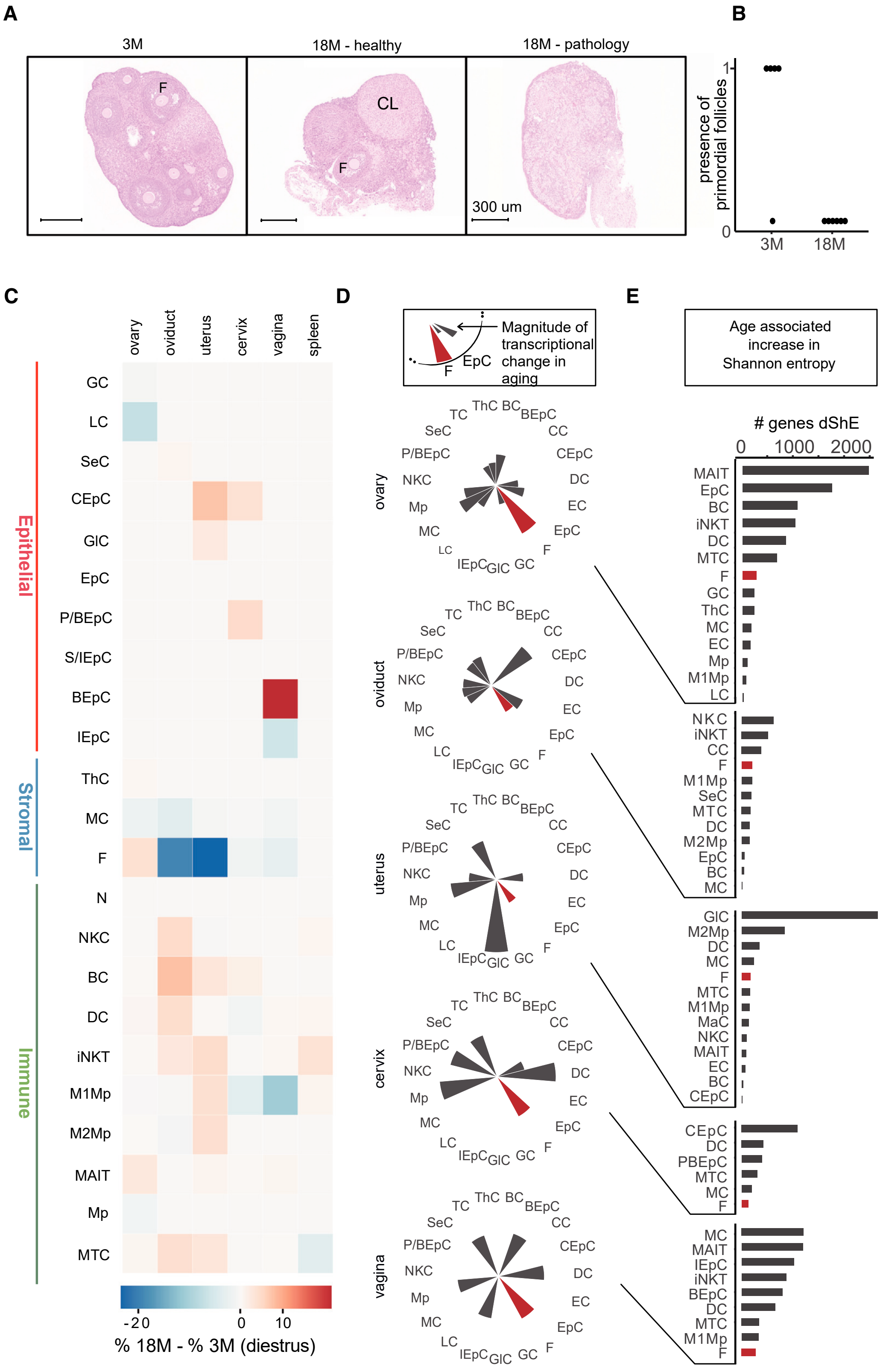

*(legend on next page)*

We tested the hypothesis that recurrent, cycle-related inflammation of fibroblasts across the reproductive lifespan might accumulate into age-related chronic inflammation. We quantified the amplitude of the organ-wide inflammation scores in young mouse fibroblasts during the cycle and compared it with age-related inflammation. The higher an organ's amplitude of inflammation is during the cycle at a young age, the higher the organ's fibroblast inflammation score will be in old age (Figure 6C). In contrast, immune cells do not display such an association (Figure 6D). Although the data are correlative, these results are in agreement with fibroblasts retaining a cumulative memory of past inflammation.

We asked whether age-related inflammation in fibroblasts is associated with altered cell-to-cell communication. Using our single-cell transcriptomics data, we found elevated inflammation activity in ligand-receptor interactions (Figure 6E). Using spatial transcriptomics data in the uterus, we found that the fraction of inflammatory signaling captured by fibroblasts increases upon aging (Figure 6F), despite a decrease in the fraction of fibroblasts (Figure 5C).

We then asked whether activated fibroblasts in the ovary and uterus form physical clusters with enhanced inflammation. We first calculated the inflammation activity scores for each SC spot in the ovary (Figure 6G). We binarized these scores into high (top 25%) and low inflammation (Figure 6H), and we constructed spatial graphs by connecting neighboring high inflammation spots (Figure 6I). We evaluated their degree of connectivity by calculating cluster coefficients. We observed that cluster sizes increase with age only in the uterus (p value = 0.046, Wilcoxon test), suggesting that foci of inflamed fibroblasts expand with age (Figure 6K).

## Tissue fibrosis accumulates with age in the oviduct, uterus, and vagina

We considered the possibility that imperfect resolution of the recurrent ECM remodeling in the estrous cycle could drive age-related accumulation of collagen underlying fibrosis. This hypothesis was partly based on two prior observations: (1) that chronic exposure of fibroblasts to inflammatory cytokines can result in collagen deposition and fibrosis[52,62] and (2) that women with more cycles have an increased risk of pathologies.[63–67]

We thus longitudinally measured intercellular collagen in FRT organs using Picrosirius red staining in 3-, 12-, 15-, 18-, and 21-month-old mice (STAR Methods). In the uterus, collagen increases most rapidly over aging (stained area increase of 3.2% per 6 months, padj $< 10^{-4}$) (Figures 7A and 7B), followed closely by the oviduct (2.7%, padj $< 10^{-3}$) and the vagina (2.3%, padj = 0.005). In contrast, the ovary and cervix do not show collagen increases (Figures 7A and 7B). Independent qualitative analysis by pathologists confirmed prevalent fibrosis in the stroma of the aged oviduct, vagina, and uterus (see Data and code availability). Signaling to fibroblasts via Tgfb is the primary driver of fibrosis in multiple organs.[38,68] Our cell-to-cell communication analysis shows that the uterus and oviduct, the two tissues with the highest rate of fibrosis development with age, also show the highest scores of Tgfb1-3 signaling to fibroblasts (Figure 2E). Interestingly, the vagina, which also has a high level of fibrosis development with age, has a low level of Tgfb signaling in young mice; however, this increases significantly with age (Figure 6E). In contrast, the ovary shows the smallest increase in fibrosis with age and also a low level of Tgfb signaling. In agreement with our conclusion that ECM gene activity in fibroblasts is best predicted by the presence of other ECM-producing fibroblasts in the neighborhood (Figures S6L–S6O), we found that fibroblasts are both top producers (Figure S5) and top consumers (Figure 3M) of Tgfb1-3 mRNA/ligand in the highly fibrotic uterus and oviduct.

## Cycling directly contributes to fibrosis

For each FRT organ, the age-related collagen accumulation rate is best predicted by the maximum phase-specific ECM activity in the cycle (Figure 7C). In other words, the intensity of ECM remodeling in fibroblasts during the estrous cycle corresponds with the severity of age-related fibrosis. Thus, intensity of ECM remodeling in each organ corresponds with the severity of fibrosis and predisposes each organ differently to fibrosis development.

Aging and cycling are intrinsically linked; to uncouple their effects on fibrosis development, we used a chemical protocol to prematurely terminate cycling in the FRT of young mice. Administration of 4-vinylcyclohexene diepoxide (VCD) causes the loss of small ovarian follicles in mice and rats, rapidly leading to acyclicity.[69]

We administered VCD to 2-month-old mice, and confirmed their acyclicity by 5 months of age. These mice were then further aged for 6 months and sacrificed at 11 months of age, in parallel with sham-injection control mice. Their uteri and oviducts were collected to assess the development of fibrosis (Figure 7D). In the uterus, fibrosis was significantly reduced in the aged VCD group, where cycling had been prematurely terminated (p value 0.032); the same general trend was observed in the oviduct (n.s.). In contrast, the control group, whose organs had both aged and cycled, showed greater fibrotic development (Figures 7E and 7F).

In sum, our results show that both aging and cycling independently contribute to fibrosis development through incompletely resolved ECM remodeling.

**Figure 5. Organ-specific impact of aging on the FRT**

(A) H&E staining of young and aged ovaries. F, follicle; CL, corpus luteum. Scale bars, 300 μm.

(B) Pathologist assessment of the presence of primordial follicles in each young and old ovary. If primordial follicles were detected in the slide, the sample was scored 1, and if no primordial follicle was present, it was scored 0. Young, n = 3; old, n = 3.

(C) Difference in average % of each cell type between aged and diestrus samples.

(D) Similarity of gene expression programs between the aged and diestrus mice for each cell type, quantified using optimal transport. Line lengths indicate magnitude of transcriptional changes. Optimal transport distances of fibroblasts are colored in red.

(E) Number of genes with increased differential Shannon entropy (ShE) of all cell types in diestrus compared with old age.

See also Figure S8.

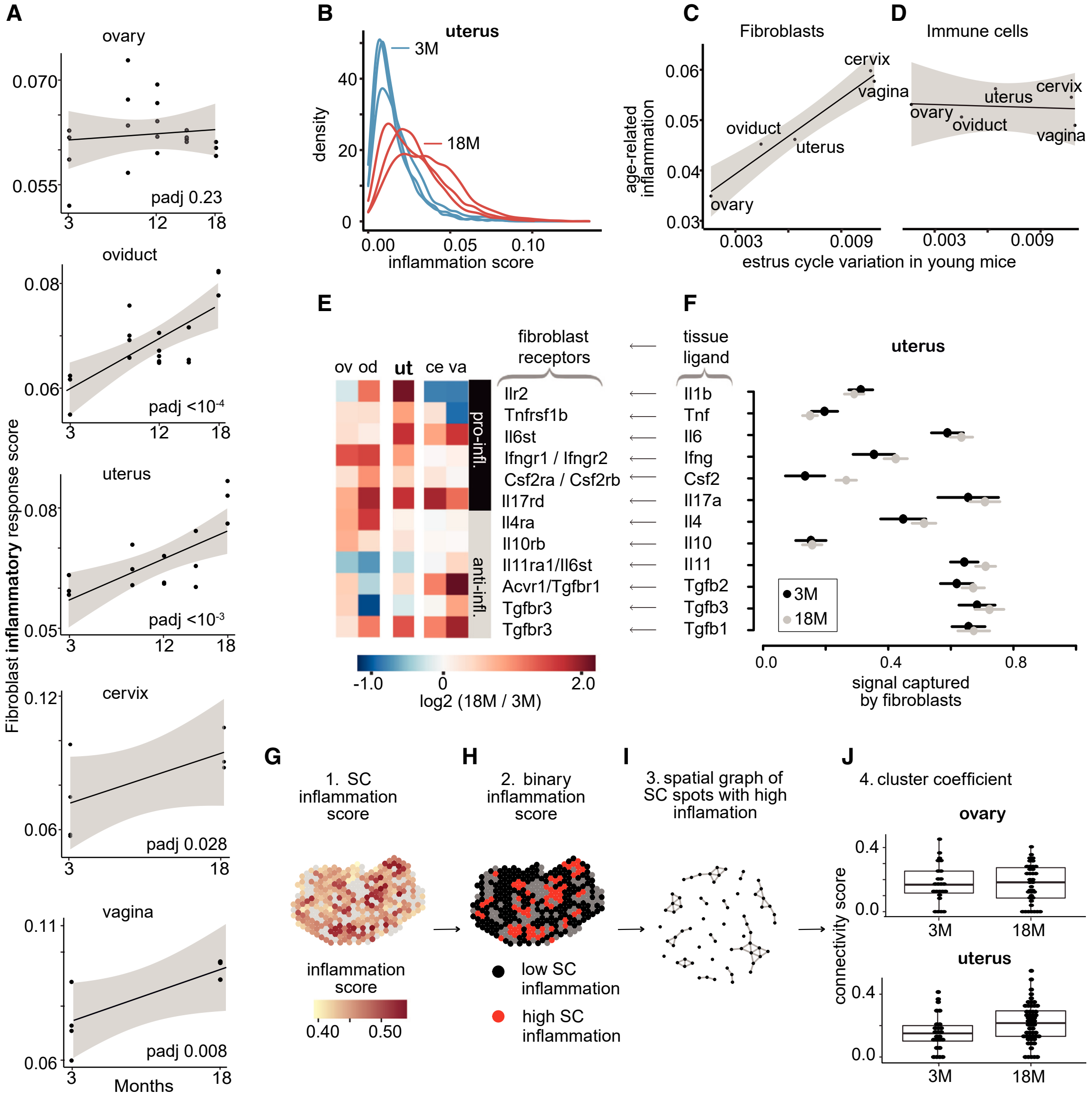

**Figure 6. Fibroblast inflammation in the FRT accumulates gradually during aging**

(A) Activity scores of inflammatory genes averaged across all fibroblasts in 3-, 9-, 12-, 15-, and 18-month-old mice in upper FRT and 3- and 18-month-old mice in lower FRT. The gray shading represents the 95% confidence level interval for predictions from a linear model (black line).

(B) Density plot of fibroblasts' inflammation scores in each biological replicate of young and old mice. p value = 0.002.

(C and D) The amplitude of variation in organ-wide inflammation in young mice (x) and the average inflammation of fibroblasts in old age (y) in fibroblasts and immune cells.

(E) $Log_2$ fold changes of inflammatory ligand-receptor products in old age compared with diestrus of all FRT organs. Ligand expression is averaged across all cell types; receptors are in fibroblasts only. (F) Ligand proportion captured by uterine fibroblasts.

(G–J) Cluster coefficient analysis used to determine the spatial distribution of inflamed fibroblast in young and old ovaries and uteruses. Ovary, p value n.s.; uterus, p value = 0.046.

(G) Fibroblasts (SC) inflammation score calculated in each ovary and uterus section.

(H) Binarized scores obtained by assigning the high inflammation label to the top 25% spots.

(I) Spatial graphs of SC spots with high inflammation labels constructed by connecting spots that are direct neighbors.

(J) Connectivity score of constructed spatial graphs of young and aged uteruses and ovaries.

## DISCUSSION

Oocyte release involves large-scale, cyclical tissue remodeling across five hormonally controlled organs in therian mammals. To better understand this system, we mapped the cellular compositional and transcriptional changes that occur during each estrous cycle phase, arising from earliest pregnancy and during aging at single-cell resolution in every organ of the mouse FRT.

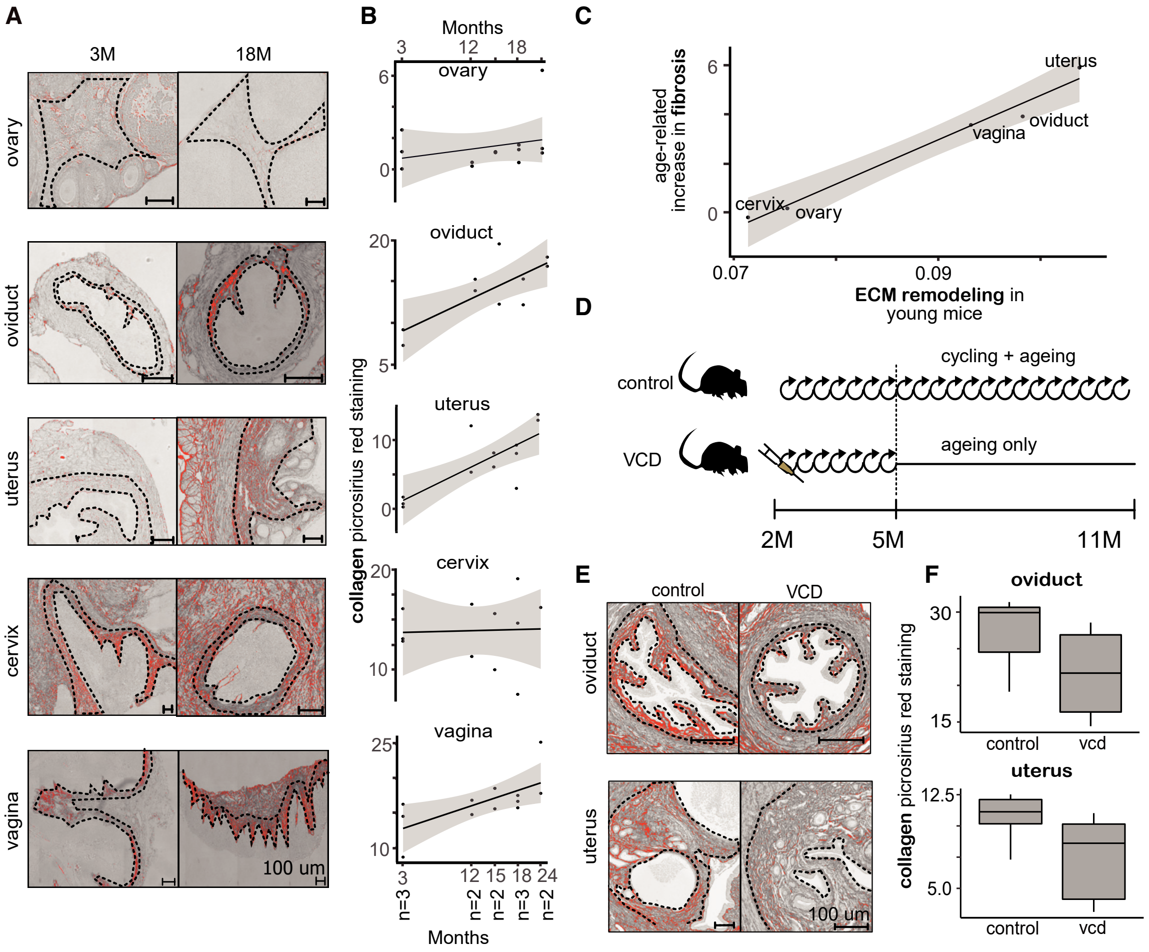

**Figure 7. Fibrosis in FRT accumulates gradually during aging**

(A) Collagen deposition in FRT tissues of 3- and 18-month-old mice. Scale bars, 300 µm.

(B) Quantification of % area of stained collagen deposition in all FRT tissues of 3-, 12-, 15-, 18-, and 21-month-old mice. Scale bars, 100 µm.

(C) The relationship between the maximum of organ-wide ECM reorganization scores of young mice during the cycle and the fibrosis score of different FRT organs in old age. Fibrosis score was calculated as the difference in % area of stained collagen in old (18 months) and young mice (3 months).

(D) Schematic representation of the VCD experiment. VCD was administered to mice at 2 months of age to stop cycling. Control group received sham injection.

(E) Collagen deposition in oviductal and uterine tissue of control and VCD-treated mice. Scale bars, 100 µm.

(F) Quantification of % area of stained collagen deposition in oviduct and uterus of control and VCD-treated mice. Oviduct: control n = 3, VCD n = 4; uterus: control n = 7, VCD n = 8. Oviduct, p value n.s.; uterus, p value = 0.032.

Our data reveal how the organs of the mouse FRT undergo recurrent drastic immune infiltration, ECM remodeling, and cell proliferation in each cycle. In most adult tissues, the ECM remodeling and cell proliferation associated with wounding leaves fibrotic scarring. However, it has long been thought that in the FRT, in particular the uterus, these events are resolved by scar-free remodeling. Instead, we find that in the uterus, oviduct, and vagina, fibrosis accumulates steadily with aging and cycling due to incomplete resolution of collagen deposition.

Here, we propose a model wherein the incomplete resolution of inflammation and ECM remodeling leads to the accumulation of cycle-related fibrosis and chronic inflammation. Such a gradual development of fibrosis and chronic inflammation would predispose organs to disease development.[70,71] We tested this hypothesis by inducing premature acyclicity to decouple estrous cycling from biological aging, thus directly demonstrating in the uterus and oviduct that reducing the number of E cycles reduces fibrotic accumulation.

How the lifetime number of reproductive cycles shapes cancer risk is an actively debated question.[64] In humans, the risk of developing endometrial carcinomas appears to be suppressed by events that reduce the number of menstrual cycles, such as continuous hormonal contraception, a larger number of pregnancies, later menarche, and early menopause.[63–65] On balance, the fewer the number of cycles, the lower the cancer risk.[66,67] To date, the molecular mechanisms underlying these epidemiological observations remain unknown. A proposed explanation is that the increase in lifetime number of menstrual cycles increases the length of time of exposure of the uterus to unopposed estrogen[72] and that unopposed estrogen may be mildly mutagenic.[73,74] Our study determined that cycling generates a detrimental microenvironment that may compound the effect of estrogen-dependent mutagenesis in the endometrium.

In sum, our atlas reveals an unexpected cost incurred by the recurrent remodeling required by the FRT for reproduction and illuminates how estrous, pregnancy, and aging together shape the FRT.

## Limitations of the study

This study is a deep characterization of how estrus cycling impacts the female reproductive tissues in mouse as a widely used model system and will be useful to guide further studies in human FRT. Differentially expressed genes in mouse uterine fibroblasts and decidual cells across the cycle and in decidualization were determined using scRNA-seq. Using these genes as markers of decidualization may require additional validation using orthogonal methods. Our major finding—that recurrent cycling contributes to fibrotic accumulation during aging—is consistent with numerous human epidemiological results but has not yet been directly confirmed in corresponding human tissues. Our study analyzes the FRT using a set of single-cell and spatial transcriptomics approaches but only indirectly addresses upstream regulation and does not analyze the impact of estrus cycling on the proteome.

## STAR★METHODS

Detailed methods are provided in the online version of this paper and include the following:

- KEY RESOURCES TABLE
- RESOURCE AVAILABILITY
    - ○ Lead contact
    - ○ Materials availability
    - ○ Data and code availability
- EXPERIMENTAL MODEL AND STUDY PARTICIPANT DETAILS
    - ○ Mouse colony management
- METHOD DETAILS
    - ○ Estrous cycle staging cytology
    - ○ Induction of decidualization
    - ○ VCD treatment
    - ○ Tissue collection and preparation
    - ○ Generation of single cell suspensions
    - ○ Histopathology and fibrosis quantification
    - ○ RNA *in situ* hybridization
    - ○ Flow cytometry staining and acquisition
    - ○ Generation of single cell transcriptomes
    - ○ Spatial transcriptomics
    - ○ Filtering and normalization of scRNA-seq data
    - ○ Cell type annotation of scRNA-seq data
    - ○ Batch correction of scRNA-seq data
    - ○ Inter-quartile range calculation
    - ○ Differential cell abundance analysis
    - ○ Optimal transport
    - ○ Differential gene expression (DGE) analysis
    - ○ Overrepresentation analysis (ORA)
    - ○ Scoring of gene set activity in single-cell RNA-seq data
    - ○ DGE analysis using Mutual-information (MI)
    - ○ Cell-to-cell communication analysis
    - ○ Spatial transcriptomics analysis
    - ○ Single-Cell Regulatory Network analysis
    - ○ Single-cell trajectory inference
    - ○ Transcriptional heterogeneity analysis
    - ○ Linear mixed models of inflammation
- QUANTIFICATION AND STATISTICAL ANALYSIS
- ADDITIONAL RESOURCES

## SUPPLEMENTAL INFORMATION

Supplemental information can be found online at https://doi.org/10.1016/j.cell.2024.01.021.

## ACKNOWLEDGMENTS

We thank the Tissue Bank of the National Center for Tumor Diseases Heidelberg, the DKFZ Single-Cell Open Lab, D. Krunic (DKFZ microscopy core), F. Blum, K. Hexel, T. Rubner, S. Schmitt, M. Eich (DKFZ flow cytometry), and the animal caretakers from ATV.108 for technical support and assistance. We thank R. Vento-Tormo, C. Berthelot, A. Krebs, L. Gahurová, and L. Doridot for offering suggestions and proofreading the manuscript. This work was supported by NCT/Helmholtz core funding (B270 to D.T.O. and B210 to A.G.), European Research Council (788937 to D.T.O.), Helmholtz junior group leader post (to A.G.), DKFZ International Fellows Program (to A.T.), and the Deutsche Forschungsgemeinschaft (FI 2558/1-1 to A.G.).

## AUTHOR CONTRIBUTIONS

Conceptualization, I.W., D.T.O., and A.G.; methodology, I.W., A.T., D.T.O., and A.G.; formal analysis, I.W., P.L., F.L., and A.G.; investigation, A.T., K.D., N.S., M.-L.K., J.P., F.G., T.P., B.M.d.A., A.S., and S.H.; data curation, I.W., A.T., and F.L.; writing – original draft, I.W., D.T.O., and A.G.; visualization, I.W., D.T.O., and A.G.; writing – review & editing, all authors; supervision, A.G. and D.T.O.; funding acquisition, A.G. and D.T.O.

## DECLARATION OF INTERESTS

The authors declare no competing interests.

Received: July 25, 2022
Revised: April 21, 2023
Accepted: January 12, 2024
Published: February 6, 2024

## REFERENCES

1. Bellofiore, N., Cousins, F., Temple-Smith, P., Dickinson, H., and Evans, J. (2018). A missing piece: the spiny mouse and the puzzle of menstruating species. J. Mol. Endocrinol. *61*, R25–R41.
2. Rajkovic, A., Pangas, S.A., Ballow, D., Suzumori, N., and Matzuk, M.M. (2004). NOBOX Deficiency Disrupts Early Folliculogenesis and Oocyte-Specific Gene Expression. Science *305*, 1157–1159.
3. Garry, R., Hart, R., Karthigasu, K.A., and Burke, C. (2010). Structural changes in endometrial basal glands during menstruation. BJOG *117*, 1175–1185.
4. Hickey, D.K., Fahey, J.V., and Wira, C.R. (2013). Mouse estrous cycle regulation of vaginal versus uterine cytokines, chemokines, α-/β-defensins and TLRs. Innate Immun. *19*, 121–131.
5. Jürgensen, A., Mettler, L., Volkov, N.I., and Parwaresch, R. (1996). Proliferative activity of the endometrium throughout the menstrual cycle in infertile women with and without endometriosis. Fertil. Steril. *66*, 369–375.

6. Sato, T., Fukazawa, Y., Kojima, H., Enari, M., Iguchi, T., and Ohta, Y. (1997). Apoptotic cell death during the estrous cycle in the rat uterus and vagina. Anat. Rec. *248*, 76–83.
7. Schulke, L., Manconi, F., Markham, R., and Fraser, I.S. (2008). Endometrial dendritic cell populations during the normal menstrual cycle. Hum. Reprod. *23*, 1574–1580.
8. Wang, H., Eriksson, H., and Sahlin, L. (2000). Estrogen receptors $\alpha$ and $\beta$ in the female reproductive tract of the rat during the estrous cycle. Biol. Reprod. *63*, 1331–1340.
9. Garcia-Alonso, L., Handfield, L.F., Roberts, K., Nikolakopoulou, K., Fernando, R.C., Gardner, L., Woodhams, B., Arutyunyan, A., Polanski, K., Hoo, R., et al. (2021). Mapping the temporal and spatial dynamics of the human endometrium in vivo and in vitro. Nat. Genet. *53*, 1698–1711.
10. Jemt, A., Sigurgeirsson, B., Hanna, A., Ujvari, D., Westgren, M., and Lundeberg, J. (2017). Comprehensive RNA sequencing of healthy human endometrium at two time points of the menstrual cycle. Biol. Reprod. *96*, 24–33.
11. Roberson, E.C., Battenhouse, A.M., Garge, R.K., Tran, N.K., Marcotte, E.M., and Wallingford, J.B. (2021). Spatiotemporal transcriptional dynamics of the cycling mouse oviduct. Dev. Biol. *476*, 240–248.
12. Saare, M., Modhukur, V., Suhorutshenko, M., Rajashekar, B., Rekker, K., Sõritsa, D., Karro, H., Soplepmann, P., Sõritsa, A., Lindgren, C.M., et al. (2016). The influence of menstrual cycle and endometriosis on endometrial methylome. Clin. Epigenetics *8*, 2.
13. Wang, W., Vilella, F., Alama, P., Moreno, I., Mignardi, M., Isakova, A., Pan, W., Simon, C., and Quake, S.R. (2020). Single cell RNAseq provides a molecular and cellular cartography of changes to the human endometrium through the menstrual cycle. Nat. Med. *26*, 1644–1653.
14. Cornet, P.B., Picquet, C., Lemoine, P., Osteen, K.G., Bruner-Tran, K.L., Tabibzadeh, S., Courtoy, P.J., Eeckhout, Y., Marbaix, E., and Henriet, P. (2002). Regulation and function of LEFTY-A/EBAF in the human endometrium. mRNA expression during the menstrual cycle, control by progesterone, and effect on matrix metalloproteinases. J. Biol. Chem. *277*, 42496–42504.
15. Von Wolff, M., Classen-Linke, I., Heid, D., Krusche, C.A., Beier-Hellwig, K., Karl, C., and Beier, H.M. (1999). Tumour necrosis factor-$\alpha$ (TNF-$\alpha$) in human endometrium and uterine secretion: An evaluation by immunohistochemistry, ELISA and semiquantitative RT-PCR. Mol. Hum. Reprod. *5*, 146–152.
16. Kim, J.M., Park, J.E., Yoo, I., Han, J., Kim, N., Lim, W.J., Cho, E.S., Choi, B., Choi, S., Kim, T.H., et al. (2018). Integrated transcriptomes throughout swine oestrous cycle reveal dynamic changes in reproductive tissues interacting networks. Sci. Rep. *8*, 5436.
17. Igarashi, T., Sato, S., Aihara, K., and Araki, T. (1995). Ultrastructural changes in the rat endometrium during the normal estrous cycle. Med. Electron Microsc. *28*, 200–209.
18. Horowitz, J.C., and Thannickal, V.J. (2019). Mechanisms for the Resolution of Organ Fibrosis. Physiology (Bethesda) *34*, 43–55.
19. Jabbour, H.N., Sales, K.J., Catalano, R.D., and Norman, J.E. (2009). Inflammatory pathways in female reproductive health and disease. Reproduction *138*, 903–919.
20. Salamonsen, L.A., Zhang, J., and Brasted, M. (2002). Leukocyte networks and human endometrial remodelling. J. Reprod. Immunol. *57*, 95–108.
21. Davidson, S., Coles, M., Thomas, T., Kollias, G., Ludewig, B., Turley, S., Brenner, M., and Buckley, C.D. (2021). Fibroblasts as immune regulators in infection, inflammation and cancer. Nat. Rev. Immunol. *21*, 704–717.
22. Kirk, T., Ahmed, A., and Rognoni, E. (2021). Fibroblast memory in development, homeostasis and disease. Cells *10*.
23. Rockey, D.C., Bell, P.D., and Hill, J.A. (2015). Fibrosis — A Common Pathway to Organ Injury and Failure. N. Engl. J. Med. *372*, 1138–1149.
24. Wilkosz, P., Greggains, G.D., Tanbo, T.G., and Fedorcsak, P. (2014). Female Reproductive Decline Is Determined by Remaining Ovarian Reserve and Age. PLoS One *9*, e108343.
25. Shirasuna, K., and Iwata, H. (2017). Effect of aging on the female reproductive function. Contracept. Reprod. Med. *2*, 23.
26. Finch, C.E., and Holinka, C.F. (1982). Aging and uterine growth during implantation in C57BL/6J mice. Exp. Gerontol. *17*, 235–241.
27. Soares, S.R., Troncoso, C., Bosch, E., Serra, V., Simón, C., Remohí, J., and Pellicer, A. (2005). Age and Uterine Receptiveness: Predicting the Outcome of Oocyte Donation Cycles. J. Clin. Endocrinol. Metab. *90*, 4399–4404.
28. Nilsson, M.E., Vandenput, L., Tivesten, Å., Norlén, A.K., Lagerquist, M.K., Windahl, S.H., Börjesson, A.E., Farman, H.H., Poutanen, M., Benrick, A., et al. (2015). Measurement of a comprehensive sex steroid profile in rodent serum by high-sensitive gas chromatography-tandem mass spectrometry. Endocrinology *156*, 2492–2502.
29. Madsen, D.H., Leonard, D., Masedunskas, A., Moyer, A., Jürgensen, H.J., Peters, D.E., Amornphimoltham, P., Selvaraj, A., Yamada, S.S., Brenner, D.A., et al. (2013). M2-like macrophages are responsible for collagen degradation through a mannose receptor-mediated pathway. J. Cell Biol. *202*, 951–966.
30. Ono, Y., Nagai, M., Yoshino, O., Koga, K., Nawaz, A., Hatta, H., Nishizono, H., Izumi, G., Nakashima, A., Imura, J., et al. (2018). CD11c+ M1-like macrophages (MΦs) but not CD206+ M2-like MΦ are involved in folliculogenesis in mice ovary. Sci. Rep. *8*, 8171.
31. Sojka, D.K., Yang, L., and Yokoyama, W.M. (2019). Uterine natural killer cells. Front. Immunol. *10*, 960.
32. Islam, E.A., Shaik-Dasthagirisaheb, Y., Kaushic, C., Wetzler, L.M., and Gray-Owen, S.D. (2016). The reproductive cycle is a pathogenic determinant during gonococcal pelvic inflammatory disease in mice. Mucosal Immunol. *9*, 1051–1064.
33. Gallichan, W.S., and Rosenthal, K.L. (1996). Effects of the estrous cycle on local humoral immune responses and protection of intranasally immunized female mice against herpes simplex virus type 2 infection in the genital tract. Virology *224*, 487–497.
34. Wood, G.A., Fata, J.E., Watson, K.L.M., and Khokha, R. (2007). Circulating hormones and estrous stage predict cellular and stromal remodeling in murine uterus. Reproduction *133*, 1035–1044.
35. Li, Q., Kannan, A., DeMayo, F.J., Lydon, J.P., Cooke, P.S., Yamagishi, H., Srivastava, D., Bagchi, M.K., and Bagchi, I.C. (2011). The Antiproliferative Action of Progesterone in Uterine Epithelium Is Mediated by Hand2. Science *331*, 912–916.
36. Kendall, R.T., and Feghali-Bostwick, C.A. (2014). Fibroblasts in fibrosis: Novel roles and mediators. Front. Pharmacol. *5*, 123.
37. DeLeon-Pennell, K.Y., Barker, T.H., and Lindsey, M.L. (2020). Fibroblasts: The arbiters of extracellular matrix remodeling. Matrix Biol. *91–92*, 1–7.
38. Meng, X.M., Nikolic-Paterson, D.J., and Lan, H.Y. (2016). TGF-$\beta$: the master regulator of fibrosis. Nat. Rev. Nephrol. *12*, 325–338.
39. Browaeys, R., Saelens, W., and Saeys, Y. (2020). NicheNet: modeling intercellular communication by linking ligands to target genes. Nat. Methods *17*, 159–162.
40. Altan-Bonnet, G., and Mukherjee, R. (2019). Cytokine-mediated communication: a quantitative appraisal of immune complexity. Nat. Rev. Immunol. *19*, 205–217.
41. Oyler-Yaniv, A., Oyler-Yaniv, J., Whitlock, B.M., Liu, Z., Germain, R.N., Huse, M., Altan-Bonnet, G., and Krichevsky, O. (2017). A Tunable Diffusion-Consumption Mechanism of Cytokine Propagation Enables Plasticity in Cell-to-Cell Communication in the Immune System. Immunity *46*, 609–620.
42. Vento-Tormo, R., Efremova, M., Botting, R.A., Turco, M.Y., Vento-Tormo, M., Meyer, K.B., Park, J.E., Stephenson, E., Polański, K.,

Goncalves, A., et al. (2018). Single-cell reconstruction of the early maternal–fetal interface in humans. Nature *563*, 347–353.

43. Finn, C.A., and Hinchliffe, J.R. (1964). Reaction of the mouse uterus during implantation and deciduoma formation as demonstrated by changes in the distribution of alkaline phosphatase. J. Reprod. Fertil. *8*, 331–338.
44. Ramathal, C.Y., Bagchi, I.C., Taylor, R.N., and Bagchi, M.K. (2010). Endometrial decidualization: Of mice and men. Semin. Reprod. Med. *28*, 17–26.
45. Soares, M.J., Müller, H., Orwig, K.E., Peters, T.J., and Dai, G. (1998). The Uteroplacental Prolactin Family and Pregnancy1. Biol. Reprod. *58*, 273–284.
46. Zhao, M., Zhang, W.Q., and Liu, J.L. (2017). A study on regional differences in decidualization of the mouse uterus. Reproduction *153*, 645–653.
47. Broekmans, F.J., Soules, M.R., and Fauser, B.C. (2009). Ovarian aging: Mechanisms and clinical consequences. Endocr. Rev. *30*, 465–493.
48. Finch, C.E. (2014). The menopause and aging, a comparative perspective. J. Steroid Biochem. Mol. Biol. *142*, 132–141.
49. Felicio, L.S., Nelson, J.F., and Finch, C.E. (1984). Longitudinal studies of estrous cyclicity in aging C57BL/6J mice: II. Cessation of cyclicity and the duration of persistent vaginal cornification. Biol. Reprod. *31*, 446–453.
50. Wang, S., Zheng, Y., Li, J., Yu, Y., Zhang, W., Song, M., Liu, Z., Min, Z., Hu, H., Jing, Y., et al. (2020). Single-Cell Transcriptomic Atlas of Primate Ovarian Aging. Cell *180*, 585–600.e19.
51. Jin, C., Wang, X., Hudgins, A.D., Gamliel, A., Pei, M., Kim, S., Contreras, D., Hoeijmakers, J., Campisi, J., Lobo, R., et al. (2022). The regulatory landscapes of human ovarian ageing. Preprint at bioRxiv.
52. Lliberos, C., Liew, S.H., Zareie, P., La Gruta, N.L., Mansell, A., and Hutt, K. (2021). Evaluation of inflammation and follicle depletion during ovarian ageing in mice. Sci. Rep. *11*, 278.
53. Craig, S.S., and Jollie, W.P. (1985). Age changes in density of endometrial stromal cells of the rat. Exp. Gerontol. *20*, 93–97.
54. Elmes, M., Szyszka, A., Pauliat, C., Clifford, B., Daniel, Z., Cheng, Z., Wathes, C., and McMullen, S. (2015). Maternal age effects on myometrial expression of contractile proteins, uterine gene expression, and contractile activity during labor in the rat. Physiol. Rep. *3*, e12305.
55. Rodriguez-Garcia, M., Patel, M.V., Shen, Z., and Wira, C.R. (2021). The impact of aging on innate and adaptive immunity in the human female genital tract. Aging Cell *20*, e13361.
56. Yaakov, T.B., Wasserman, T., and Savir, Y. (2021). Aged mouse ovarian immune milieu shows a shift towards adaptive immunity and attenuated cell function. Preprint at bioRxiv.
57. Kimmel, J.C., Penland, L., Rubinstein, N.D., Hendrickson, D.G., Kelley, D.R., and Rosenthal, A.Z. (2019). Murine single-cell RNA-seq reveals cell-identity- and tissue-specific trajectories of aging. Genome Res. *29*, 2088–2103.
58. Enge, M., Arda, H.E., Mignardi, M., Beausang, J., Bottino, R., Kim, S.K., Quake, S.R., Enge, M., Arda, H.E., Mignardi, M., et al. (2017). Single-Cell Analysis of Human Pancreas Reveals Transcriptional Signatures of Aging and Somatic Article Single-Cell Analysis of Human Pancreas Reveals Transcriptional Signatures of Aging and Somatic Mutation Patterns. Cell *171*, 321–323.e14.
59. Martinez-Jimenez, C.P., Eling, N., Chen, H., Vallejos, C.A., Kolodziejczyk, A.A., Connor, F., Stojic, L., Rayner, T.F., Stubbington, M.J.T., Teichmann, S.A., et al. (2017). Aging increases cell-to-cell transcriptional variability upon immune stimulation. Science *1436*, 1433–1436.
60. Horvath, S. (2013). DNA methylation age of human tissues and cell types. Genome Biol. *14*, R115.
61. Schefzik, R., Flesch, J., and Goncalves, A. (2021). Fast identification of differential distributions in single-cell RNA-sequencing data with waddR. Bioinformatics *37*, 3204–3211.
62. Selman, M., and Pardo, A. (2021). Fibroageing: An ageing pathological feature driven by dysregulated extracellular matrix-cell mechanobiology. Ageing Res. Rev. *70*, 101393.
63. Havrilesky, L.J., Moorman, P.G., Lowery, W.J., Gierisch, J.M., Coeytaux, R.R., Urrutia, R.P., Dinan, M., McBroom, A.J., Hasselblad, V., Sanders, G.D., et al. (2013). Oral Contraceptive Pills as Primary Prevention for Ovarian Cancer: A Systematic Review and Meta-analysis. Obstet. Gynecol. *122*, 139–147.
64. Iversen, L., Sivasubramaniam, S., Lee, A.J., Fielding, S., and Hannaford, P.C. (2017). Lifetime cancer risk and combined oral contraceptives: the Royal College of General Practitioners' Oral Contraception Study. Am. J. Obstet. Gynecol. *216*, 580.e1–580.e9.
65. Michels, K.A., Pfeiffer, R.M., Brinton, L.A., and Trabert, B. (2018). Modification of the Associations Between Duration of Oral Contraceptive Use and Ovarian, Endometrial, Breast, and Colorectal Cancers. JAMA Oncol. *4*, 516–521.
66. Gavrilyuk, O., Braaten, T., Weiderpass, E., Licaj, I., and Lund, E. (2018). Lifetime number of years of menstruation as a risk index for postmenopausal endometrial cancer in the Norwegian Women and Cancer Study. Acta Obstet. Gynecol. Scand. *97*, 1168–1177.
67. D'Urso, S., Arumugam, P., Weider, T., Hwang, L.D., Bond, T.A., Kemp, J.P., Warrington, N.M., Evans, D.M., O'Mara, T.A., and Moen, G.H. (2022). Mendelian randomization analysis of factors related to ovulation and reproductive function and endometrial cancer risk. BMC Med. *20*, 419.
68. Kim, K.K., Sheppard, D., and Chapman, H.A. (2018). TGF-$\beta$1 Signaling and Tissue Fibrosis. Cold Spring Harb. Perspect. Biol. *10*, a022293.
69. Brooks, H.L., Pollow, D.P., and Hoyer, P.B. (2016). The VCD Mouse Model of Menopause and Perimenopause for the Study of Sex Differences in Cardiovascular Disease and the Metabolic Syndrome. Physiology (Bethesda) *31*, 250–257.
70. Dossus, L., Lukanova, A., Rinaldi, S., Allen, N., Cust, A.E., Becker, S., Tjonneland, A., Hansen, L., Overvad, K., Chabbert-Buffet, N., et al. (2013). Hormonal, Metabolic, and Inflammatory Profiles and Endometrial Cancer Risk Within the EPIC Cohort—A Factor Analysis. Am. J. Epidemiol. *177*, 787–799.
71. Pradip, D., Jennifer, A., and Nandini, D. (2021). Cancer-Associated Fibroblasts in Conversation with Tumor Cells in Endometrial Cancers: A Partner in Crime. Int. J. Mol. Sci. *22*, 9121.
72. O'Connor, K.A., Ferrell, R.J., Brindle, E., Shofer, J., Holman, D.J., Miller, R.C., Schechter, D.E., Singer, B., and Weinstein, M. (2009). Total and Unopposed Estrogen Exposure across Stages of the Transition to Menopause. Cancer Epidemiol. Biomarkers Prev. *18*, 828–836.
73. Liehr, J.G. (2000). Is Estradiol a Genotoxic Mutagenic Carcinogen? Endocr. Rev. *21*, 40–54.
74. Moore, L., Leongamornlert, D., Coorens, T.H.H., Sanders, M.A., Ellis, P., Dentro, S.C., Dawson, K.J., Butler, T., Rahbari, R., and Mitchell, T.J. (2018). The mutational landscape of normal human endometrial epithelium. Nature *580*, 640–646.
75. Hao, Y., Hao, S., Andersen-Nissen, E., Mauck, W.M., Zheng, S., Butler, A., Lee, M.J., Wilk, A.J., Darby, C., Zager, M., et al. (2021). Integrated analysis of multimodal single-cell data. Cell *184*, 3573–3587.e29.
76. McCarthy, D.J., Campbell, K.R., Lun, A.T., and Wills, Q.F. (2017). Scater: pre-processing, quality control, normalization and visualization of single-cell RNA-seq data in R. Bioinformatics *33*, 1179–1186.
77. Lun, A.T.L., and Marioni, J.C. (2016). Overcoming confounding plate effects in differential expression analyses of single-cell RNA-seq data. Biostatistics *18*, 451–464.
78. Pliner, H.A., Shendure, J., and Trapnell, C. (2019). Supervised classification enables rapid annotation of cell atlases. Nat. Methods *16*, 983–986.
79. Meyer, D., Dimitriadou, E., Hornik, K., Weingessel, A., and Leisch, F. (2023). e1071: misc functions of the department of statistics, probability theory

group (formerly: E1071). https://cran.r-project.org/web/packages/e1071/e1071.pdf.

80. Frauhammer, F., and Anders, S. (2022). cellpypes: Cell Type Pipes for R. Version 0.1.1 (Zenodo. https://zenodo.org/records/6555728.
81. Van Den Boogaart, K.G., and Tolosana-Delgado, R. (2008). "compositions": A unified R package to analyze compositional data. Comput. Geosci. *34*, 320–338.
82. Bates, D., Mächler, M., Bolker, B., and Walker, S. (2014). Fitting Linear Mixed-Effects Models Using lme4. J. Stat. Softw. *67*, 1–48.
83. Brooks, M.E., Kristensen, K., van Benthem, K.J., Magnusson, A., Berg, C.W., Nielsen, A., Skaug, H.J., Machler, M., and Bolker, B.M. (2017). glmmTMB balances speed and flexibility among packages for zero-inflated generalized linear mixed modeling. R J. *9*, 378–400.
84. Lopez, R., Li, B., Keren-Shaul, H., Boyeau, P., Kedmi, M., Pilzer, D., Jelinski, A., Yofe, I., David, E., Wagner, A., et al. (2022). DestVI identifies continuums of cell types in spatial transcriptomics data. Nat. Biotechnol. *40*, 1360–1369.
85. Barton, K., and Barton, M.K. (2015). Package 'mumin.'. Version 1*439*.
86. Van de Sande, B., Flerin, C., Davie, K., De Waegeneer, M., Hulselmans, G., Aibar, S., Seurinck, R., Saelens, W., Cannoodt, R., Rouchon, Q., et al. (2020). A scalable SCENIC workflow for single-cell gene regulatory network analysis. Nat. Protoc. *15*, 2247–2276.
87. Street, K., Risso, D., Fletcher, R.B., Das, D., Ngai, J., Yosef, N., Purdom, E., and Dudoit, S. (2018). Slingshot: cell lineage and pseudotime inference for single-cell transcriptomics. BMC Genomics *19*, 477.
88. Hastie, M.T. (2017). Package 'mda.'. CRAN R Proj.
89. Wang, K., Phillips, C.A., Saxton, A.M., and Langston, M.A. (2015). EntropyExplorer: an R package for computing and comparing differential Shannon entropy, differential coefficient of variation and differential expression. BMC Res. Notes *8*, 832.
90. Delignette-Muller, M.L., and Dutang, C. (2015). fitdistrplus: An R package for fitting distributions. J. Stat. Softw. *64*, 1–34.
91. Liberzon, A., Birger, C., Thorvaldsdóttir, H., Ghandi, M., Mesirov, J.P., and Tamayo, P. (2015). The Molecular Signatures Database (MSigDB) Hallmark Gene Set Collection. Cell Syst. *1*, 417–425.
92. Ramakrishnan, K., Grey, B., and Haesun, P. (2016). A high-performance parallel algorithm for nonnegative matrix factorization. In Proceedings of the 21st ACM SIGPLAN Symposium on Principles and Practice of Parallel Programming, *9*, pp. 1–11. PPoPP 16.
93. Schneider, C.A., Rasband, W.S., and Eliceiri, K.W. (2012). NIH Image to ImageJ: 25 years of image analysis. Nat. Methods *9*, 671–675.
94. Lachmann, A., Giorgi, F.M., Lopez, G., and Califano, A. (2016). ARACNe-AP: gene network reverse engineering through adaptive partitioning inference of mutual information. Bioinformatics *32*, 2233–2235.
95. Aibar, S., González-Blas, C.B., Moerman, T., Huynh-Thu, V.A., Imrichova, H., Hulselmans, G., Rambow, F., Marine, J.C., Geurts, P., Aerts, J., et al. (2017). SCENIC: single-cell regulatory network inference and clustering. Nat. Methods *14*, 1083–1086.
96. Jin, S., Guerrero-Juarez, C.F., Zhang, L., Chang, I., Ramos, R., Kuan, C.H., Myung, P., Plikus, M.V., and Nie, Q. (2021). Inference and analysis of cell-cell communication using CellChat. Nat. Commun. *12*, 1088.
97. Shao, X., Liao, J., Li, C., Lu, X., Cheng, J., and Fan, X. (2021). CellTalkDB: a manually curated database of ligand–receptor interactions in humans and mice. Brief. Bioinform. *22*, bbaa269.
98. Byers, S.L., Wiles, M.V., Dunn, S.L., and Taft, R.A. (2012). Mouse Estrous Cycle Identification Tool and Images. PLoS One *7*, e35538.
99. Parker, G.A., and Picut, C.A. (2016). Atlas of Histology of the Juvenile Rat (Academic Press).
100. Brunet, J.P., Tamayo, P., Golub, T.R., and Mesirov, J.P. (2004). Metagenes and molecular pattern discovery using matrix factorization. Proc. Natl. Acad. Sci. USA *101*, 4164–4169.
101. Korsunsky, I., Wei, K., Pohin, M., Kim, E.Y., Barone, F., Major, T., Taylor, E., Ravindran, R., Kemble, S., Watts, G.F.M., et al. (2022). Cross-tissue, single-cell stromal atlas identifies shared pathological fibroblast phenotypes in four chronic inflammatory diseases. Med. *3*, 481–518.e14.
102. Ajayi, A.F., and Akhigbe, R.E. (2020). Staging of the estrous cycle and induction of estrus in experimental rodents: an update. Fertil. Res. Pract. *6*, 5.
103. Greaves, P. (2012). Female Genital Tract. Chapter 12. In Histopathology of Preclinical Toxicity Studies, Fourth Edition, P. Greaves, ed. (Academic Press), pp. 667–723.
104. Efremova, M., Vento-Tormo, M., Teichmann, S.A., and Vento-Tormo, R. (2020). CellPhoneDB: inferring cell–cell communication from combined expression of multi-subunit ligand–receptor complexes. Nat. Protoc. *15*, 1484–1506.
105. Gurtner, G.C., Werner, S., Barrandon, Y., and Longaker, M.T. (2008). Wound repair and regeneration. Nature *453*, 314–321.
106. Koliaraki, V., Prados, A., Armaka, M., and Kollias, G. (2020). The mesenchymal context in inflammation, immunity and cancer. Nat. Immunol. *21*, 974–982.
107. Turner, M.D., Nedjai, B., Hurst, T., and Pennington, D.J. (2014). Cytokines and chemokines: At the crossroads of cell signalling and inflammatory disease. Biochim. Biophys. Acta *1843*, 2563–2582.

## STAR★METHODS

### KEY RESOURCES TABLE

| REAGENT or RESOURCE | SOURCE | IDENTIFIER |
|---|---|---|
| Antibodies | | |
| F4/80:PB | Invitrogen | Cat#MF48028; RRID: AB_10373419 |
| NK1.1:BV785 | BioLegend | Cat#108749; Clone PK136; RRID: AB_2564304 |
| CD11C:PE-Cy7 | BioLegend | Cat#117317; Clone: N418; RRID: AB_493569 |
| CD11b:APC | eBioscience | Cat# 25-0112; Clone: M1/70; RRID: AB_469588 |
| CD45:AF700 | Invitrogen | Cat#56-0451-82; Clone: 30-F11; RRID: RRID AB_891454 |
| Anti-alpha smooth muscle actin | Abcam | Cat#ab5694; RRID: AB_2223021 |
| Anti-Desmin | Thermo scientific | Cat#RB-9014-Po; RRID: AB_149768 |
| Anti-Cytokeratin | Dako /Agilent | Cat#Z0622; RRID: AB_2650434 |
| Gr1:APC-eF786 | eBioscience | Cat#RB6-8C5; RRID: AB_1074825 |
| Chemicals, peptides, and recombinant proteins | | |
| Viability Dye eF506 | eBioscience | Cat#65-0866-14 |
| Propidium iodide solution (1,0 mg/ml) | Invitrogen | Cat#P3566 |
| Tissue-Tek® O.C.T. Compound | Sakura Finetek | Cat#4583 |
| DAPI | Invitrogen | Cat#D3571 |
| Collagenase I | Worthington | Cat#LS0004194 |
| Collagenase II | Worthington | Cat#LS0004174 |
| Collagenase IV | Worthington | Cat#LS0004186 |
| Bovine hyaluronidase (from Testes) | VWR | Cat#SIALH3884 |
| Crystal violet | Sigma-Aldrich | Cat#61135 |
| 4-vinylcyclohexene diepoxide | Sigma-Aldrich | Cat#94956-100ML |
| Sesame oil | Sigma-Aldrich | Cat#S3547-250ML |
| Fast panotic coloring set | Laborclin | Cat#620529 |
| Paraformaldehyde | Dinamica | Cat#P.10.0804.000.00 |
| Picro-Sirius red | Morphisto | Cat#13422.00500 |
| Giemsa’s Azur-Eosin-Methylenblue | Sigma Aldrich | Cat# 1.09204.0500 |
| AFOG | Morphisto | Cat#11881.0010 |
| Kongored 0,5 % in Ethanol 50 % | Morphisto | Cat# 11794.00100 |
| Hematoxylin solution modified according to Gill III | Merck | Cat#105174 |
| Eosin Y | Merck | Cat#1.15935.0100 |
| Panoptical staining | Carl Roth | Cat#6487.1 |
| Formalin solution, neutral buffered 10% | Sigma-Aldrich | Cat#HT501128-4L |
| ProLong™ Gold Antifade Mountant with DNA Stain DAPI | Invitrogen | Cat#P36931 |
| Opal dyes 520, 570 and 690 | Akoya Biosciences | Cat#FP1487001KT |
| Critical commercial assays | | |
| Chromium Single Cell 3’ Reagent Kit v3.0 and Chromium Next GEM Single Cell 3′ Reagents Kits v3.1 | 10X Genomics | Cat#PN-1000075 and Cat#PN-1000121 |
| Single Index Kit T Set A | 10X Genomics | Cat#PN-1000213 |
| Dual Index Kit TT Set A | 10X Genomics | Cat#PN-1000215 |
| Visium Spatial Gene Expression Slide & Reagents Kit | 10X Genomics | Cat#PN-1000184 |

(*Continued on next page*)

*Continued*

| REAGENT or RESOURCE | SOURCE | IDENTIFIER |
|---|---|---|
| RNAScope Multiplex Fluorescent V2 Assay | ACD | Cat#323100 |
| Deposited data | | |
| Sequencing raw and analyzed data of the mouse FRT tissues across estrous cycle and aging (ovary, oviduct, uterus, cervix and vagina) and decidualization (uterus) using 10x scRNA-seq | This paper | Arrayexpress: E-MTAB-11491, E-MTAB-12889 |
| Sequencing raw and analyzed data of the young and old mouse ovaries and uterus using 10x Visium | This paper | Arrayexpress: E-MTAB-12105 |
| Imaging raw and processed data | This paper | Biostudies: S-BIAD482, S-BIAD476 |
| Flow cytometry raw data | This paper | Biostudies: S-BSST864 |
| Sequencing raw and analyzed data of the human endometrium across menstrual cycle | Wang et al.[13] | GEO: GSE111976 |
| Experimental models: Organisms/strains | | |
| Mouse: C57BL/6JRj | Janvier Labs | Cat#B6J |
| Mouse: C57BL/6Ly5.1 | Charles Rivers | Cat#B6.SJL-PtprcaPepcb/BoyCrl |
| Mouse: C57BL/6N | Charles Rivers | Cat#B6N |
| Mouse: C57BL/6 | Central Vivarium, Universidade Federal de Pelotas | N/A |
| Oligonucleotides | | |
| RNAScope probe Col1a1 | ACD | Cat#319371-C1 |
| RNAscope 3-plex Negative Control Probe | ACD | Cat#320871 |
| Software and algorithms | | |
| Cellranger | 10X Genomics | https://support.10xgenomics.com/single-cell-gene-expression/software/overview/welcome |
| Seurat | Hao et al.[75] | https://cran.r-project.org/web/packages/Seurat/index.html |
| Scater | McCarthy et al.[76] | https://bioconductor.org/packages/release/bioc/html/scater.html |
| Scran | Lun[77] | https://bioconductor.org/packages/release/bioc/html/scran.html |
| Garnett | Pliner et al.[78] | https://cole-trapnell-lab.github.io/garnett/docs/ |
| e1071 | Meyer et al.[79] | https://cran.r-project.org/web/packages/e1071/index.html |
| kNN pooling | Frauhammer and Anders[80] | https://cran.r-project.org/web/packages/cellpypes/cellpypes.pdf |
| Compositions | Van Den Boogaart and Tolosana-Delgado[81] | https://cran.r-project.org/web/packages/compositions/index.html |
| lme4 | Bates et al.[82] | https://cran.r-project.org/web/packages/lme4/index.html |
| NicheNet | Browaeys et al.[39] | https://github.com/saeyslab/nichenetr |
| glmmTMB | Brooks et al.[83] | https://cran.r-project.org/web/packages/glmmTMB/index.html |
| DestVI | Lopez et al.[84] | https://pypi.org/project/scvi-colab/ |
| MuMIn | Barton and Barton[85] | https://cran.r-project.org/web/packages/MuMIn/index.html |
| pySCENIC | Van de Sande et al.[86] | https://pypi.org/project/pyscenic/ |
| Slingshot | Street et al.[87] | https://bioconductor.org/packages/release/bioc/html/slingshot.html |
| Mda | Hastie[88] | https://cran.r-project.org/web/packages/mda/index.html |

(*Continued on next page*)

***Continued***

| REAGENT or RESOURCE | SOURCE | IDENTIFIER |
|---|---|---|
| EntropyExplorer | Wang et al.[89] | http://cran.nexr.com/web/packages/EntropyExplorer/index.html |
| Fitdistrplus | Delignette-Muller and Dutang[90] | https://cran.r-project.org/web/packages/fitdistrplus/index.html |
| MsigDB | Liberzon et al.[91] | https://www.gsea-msigdb.org/gsea/msigdb/ |
| PLANC | Ramakrishnan et al.[92] | https://github.com/ramkikannan/planc |
| ImageJ | Schneider et al.[93] | https://imagej.net/ij/download.html |
| Spaceranger | 10X Genomics | https://www.10xgenomics.com/support/software/space-ranger |
| ARACNe-AP | Lachmann et al.[94] | https://github.com/califano-lab/ARACNe-AP |
| BD FACSDiva Software | BD Biosciences | https://www.bdbiosciences.com/en-us/products/software/instrument-software/bd-facsdiva-software |
| AUCell | Aibar et al.[95] | https://bioconductor.org/packages/release/bioc/html/AUCell.html |
| FlowJo | BD Biosciences | https://www.bdbiosciences.com/en-us/products/software/flowjo-v10-software |
| CellChatDB | Jin et al.[96] | www.cellchat.org/cellchatdb |
| CellTalkDB | Shao et al.[97] | https://github.com/ZJUFanLab/CellTalkDB |
| Original code used to perform scRNA-seq and spatial transcriptomics analyses | This paper | https://doi.org/10.5281/zenodo.10259662 |
| Other | | |
| Interactive tool for exploring dynamics of cellular abundance, gene expression, cell-to-cell communication and transcription factor regulatory networks in female reproductive tract | This paper | https://cancerevolution.dkfz.de/estrus/ |

## RESOURCE AVAILABILITY

### Lead contact

Further information and requests for resources and reagents should be directed to and will be fulfilled by the lead contact, Angela Goncalves (a.goncalves@dkfz-heidelberg.de).

### Materials availability

This study did not generate new unique reagents.

### Data and code availability

All sequencing data (10x scRNA-seq and 10x Visium) and expression count matrices (10x scRNA-seq) are deposited in ArrayExpress and are publicly available as of the date of publication. All accession numbers are listed in the Key resources table. Imaging raw and processed data, and pathology reports are available in Biostudies. Flow cytometry raw data and the MIFlowCyt protocol are available in Biostudies. Results of scRNA-seq and spatial transcriptomics analysis are available at Biostudies. All accession numbers are listed in the Key resources table. Dynamics of cellular abundance, gene expression, cell-to-cell communication and transcription factor regulatory networks in FRT organs in estrous cycle, decidualization and aging, can be explored through an interactive tool at https://cancerevolution.dkfz.de/estrus/. This paper analyzes existing, publicly available data, the accession number is listed in the Key resources table.

All original code has been deposited at Zenodo and is publicly available as of the date of publication. DOIs are listed in the Key resources table.

Any additional information required to reanalyze the data reported in this paper is available from the Lead contact upon request.

## EXPERIMENTAL MODEL AND STUDY PARTICIPANT DETAILS

### Mouse colony management

The C57BL/6 substrains J, N and Ly5.1 were obtained from Charles Rivers or Janvier. This study used only female mice. Mice ages ranged from 3 months to 18 months of age. Exact ages, treatment and mouse strain information are listed in Table S1. Females were maintained as virgins and housed in groups of up to six mice in Tecniplast GM500 IVC cages with a 12-hour light / 12-hour dark cycle. Mice had *ad libitum* access to water, food (Kliba 3437), and environmental enrichments. All colonies were regularly controlled for infections using sentinel mice to ensure a healthy status. None of the animals were involved in previous procedures. All experiments were carried out in accordance with and approval of the German Cancer Research Center ethical committee and local governmental regulations (Regierungspräsidium Karlsruhe, animal license number DKFZ366). VCD experiment procedures were approved by the Ethics Committee of the Federal University of Pelotas (UFPel). All female mice were randomly assigned to experimental groups.

## METHOD DETAILS

### Estrous cycle staging cytology

Vaginal smears were collected using a pasteur pipette containing PBS and leaned towards or inserted in the vagina of the restrained mouse. Mucous tissue was then trickled on dry glass slides and stained by crystal violet staining solution (Sigma-Aldrich 61135) or panoptic staining (Carl Roth 6487.1). Cellular composition of the smears was analyzed according to known cell distribution patterns[98] using a ZEISS Discovery.V12 Stereoscope and images were acquired via a ZEISS Cell Observer® system with AxioCam MRc camera. If possible, smears were collected and analyzed from multiple consecutive days to better estimate estrous cycle course. On the day of tissue collection, estimation of the estrous cycle phase by smears was further complemented by the state of the vaginal opening and the thickness and vascularization of the uterine horns.[99]

### Induction of decidualization

Three month old female C57BL/6J virgin mice were synchronized 3 days prior to mating by housing in cages containing bedding from C57BL/6 male mice. These females were allowed to mate with C57BL/6 males in one to one matings overnight. On the following morning, all plug-positive females were housed together and kept for 5 days (5.5 days post coitum) until sacrifice for organ harvesting. On average, two out of three plug-positive mice were pregnant at the day of sacrifice. Two uterine pieces, each enveloping an implanted embryo were removed per mouse and further processed for 10x or histology as described below.

### VCD treatment

At 60 days of age, C57BL/6 mice in VCD group received 4-vinylcyclohexene diepoxide (VCD; Sigma-Aldrich; i.p.; 160 mg/kg) diluted in sesame oil for 20 consecutive days.[69] The control group received sesame oil i.p. injections as placebo. At 5 months of age mice were submitted to vaginal cytology analysis for 5 consecutive days. We confirmed that 100% of the females in the VCD group were not cyclic. Females were euthanized at 11 months of age to collect oviducts and uteruses, which were stored in 10% paraformaldehyde solution.

### Tissue collection and preparation

Ovaries, oviducts, uteruses, cervices, vaginas, and spleens from 3 month old mice in all four phases of the estrous cycle were collected in triplicate. Same tissues were collected from 18 month old mice in quintuplicate. Seven replicates were collected for decidualized uteruses. Additional biological replicates for samples that failed QC requirements were generated as deemed necessary. No sample size estimation was performed. Samples "Ind001-vagina06" and "Ind001-uterus07", "18mo_Ind001-ovary01", "18mo_Ind001-spleen01" and "18mo_Ind001-ovary02" were excluded from the analysis due to problematic sample preparation. Instead, additional mice were sacrificed to collect the vagina in proestrus ("Ind001-vagina13"), uterus in diestrus ("Ind001-uterus16"), ovary from 18 month old mice ("18mo_Ind001-ovary04", "18mo_Ind001-ovary05") and spleen "18mo_Ind001-spleen05". Reproductive tract organs and spleen were collected from mice immediately following cervical dislocation. All organs were manually dissected using a ZEISS Discovery.V12 Stereoscope to remove surrounding fat and connective tissue. Samples were then either processed by enzymatic digestion for single cell sequencing, fixed in 10% formalin for FFPE-histology, or fixed and slowly frozen in O.C.T. Medium (ThermoFisher) for cryo-histology.

### Generation of single cell suspensions

To generate single cell suspensions, freshly isolated whole organs including ovary, oviduct and tissue pieces from uterus, cervix, vagina and spleen were treated by enzymatic digestion. All tissues were initially incubated separately in 2 ml Eppendorf tubes containing 600 μl of 0,25% trypsin in HBSS and digested at 37°C with gentle rocking. After 30 minutes, 600μL of a second digestion buffer containing Collagenase I (1.25 mg/mL), II (0.5 mg/mL), IV (0.5 mg/mL), and Hyaluronidase (0.1 mg/uL) in HBSS was added for another 2 hours. After quenching the digestion by adding 600μL HBSS with 10% FBS, the cell suspensions were passed through a 40μm cell strainer (Greiner Bio One) to remove cell debris and buffer residue. Cell suspensions were gently centrifuged at 350g for 8 min at 4°C. Cells were resuspended in PBS containing 0,04% BSA, 1 mM EDTA and propidium iodide (PI) was added to final concentration of

1 μg/ml prior to fluorescence-activated cell sorting (FACS). Larger cells such as oocytes and smooth muscle cells were excluded in the cell straining step.

### Histopathology and fibrosis quantification

After overnight fixation in 10% buffered formalin, representative specimens of the ovary, oviduct, uterus, cervix, vagina, and spleen, together with control and VCD-treated oviducts and uteruses were routinely dehydrated, embedded in paraffin, and cut into 4 μm-thick sections. All tissue sections were stained using a H&E standard protocol. Briefly, tissues were deparaffinized using xylene and rehydrated in ethanol and distilled water. Sections were then stained in Gill-hematoxylin, rinsed with water and counterstained with eosin, followed by dehydration and air-drying. In selected tissue sections, a Giemsa, Picrosirius Red, Congo Red, and AFOG (Acid Fuchsin Orange G) stain were performed according to respective standard protocols. Giemsa staining was performed using 20% Giemsa stain for 20 min, differentiating slides in acidified water, followed by ethanol, isopropanol and xylene and air-drying samples. To perform Picro-sirius Red staining, tissues were deparaffinized using xylene, rehydrated in ethanol and distilled water and incubated in Picro-sirius Red solution for 1 hour. This was followed by washing with two changes of acetic acid water, dehydration with ethanol and clearing with xylene. To perform Congo Red staining, sections were deparaffinized and hydrated. Samples were then stained using Weigert's hematoxylin for 3 mins, submerged in tap water for 3 mins, differentiated in HCl alcohol and again submerged in tap water for 3 mins. Sections were then stained in Congo red solution for 20 minutes, dehydrated with ethanol and cleared with xylene. For AFOG staining, slides were deparaffinized in xylol and rehydrated in ethanol and distilled water. Slides were incubated in Bouin's solution for 1 h at 60°C, followed by wash in tap water. Slides were then stained using Weigert's hematoxylin for 2 mins, differentiated in HCl alcohol, submerged in tap water for 3 mins and incubated in 1% phosphomolybdic acid. After washing in running distilled water slides were stained with AFOG and dehydrated with ethanol and xylol. Step-by-step protocols are available in Biostudies (see key resources table). To detect potential tumors, tumor classification immunohistochemistry was performed with anti-a smooth muscle actin (Abcam, ab5694), anti-desmin (ThermoFisher, RB-9014-Po), and anti-pan-cytokeratin (DAKO, Z0622). Whole-slide scans were acquired using the Aperio AT2 slide scanner (Leica) at 40x resolution. Raw image files are available from BioStudies (see data and code availability). To quantify fibrosis in longitudinal aging study, high-resolution whole tissue section images of Picrosirius red stained samples were acquired at 20x using a ZEISS Cell Observer® brightfield microscope and an AxioCam MRc camera. Whole tissue images of control and VCD samples were acquired using the Aperio AT2 slide scanner (Leica) at 40x resolution. Fiji software[93] (ImageJ ver. 1.53f51) was used to quantify percent of fibrotic area by setting a signal threshold in stroma-containing regions. RGB images were split into three channels. Signal quantification was performed on the green channel. Threshold was set to correspond with the fibrotic area previously assessed by a pathologist and regions of interest were drawn around stroma areas. Collagen accumulations were defined as % of area with positive signal. The macro is available from the GitHub repository (data and code availability).

In the aging study, two replicates were used for 12, 15 and 21 month old mice, and three replicates were used for 3 and 18 month old mice. No sample size estimation was performed. Analyses were performed independently by two authors (I.W. and A.T.) to reduce stroma area selection bias. Technical replicates or quantified regions of interest from the same sample were averaged and treated as one biological replicate in a linear regression model. Model was fitted under beta distribution using the glmmTMB package[83] (v 1.1.5). P-values were corrected for multiple testing using Benjamini-Hochberg procedure.

Wilcoxon test was used to test if VCD group and control group show significant difference in % area with collagen depositions.

### RNA *in situ* hybridization

To detect and quantify Collagen, Type 1, alpha 1 (Col1a1, ACD 319371) mRNA, an ISH was performed using the RNAScope Multiplex Fluorescent V2 Assay (ACD 323100) with Opal fluorophore reagents (Akoya Biosciences). Collected fresh and fixed frozen samples were cut at 10μm thickness using a Leica CM3050S cryotome. Target probes (Col1a1, 319371-C1) were applied to the sample and baked at 40°C for 2h. Opal dyes 520 (FP1487001KT), 570 (FP1488001KT) and 690 (FP1497001KT) were applied at a 1:1000 to 1:750 dilution and counterstained with DAPI. Images were taken using the ZEISS Cell Observer® fluorescence microscope and a ZEISS AxioCam MRm camera at 20x resolution.

Collagen signal was quantified as percent area of total DAPI area using ImageJ (v *1.53t*). Samples which were run with negative control probes (ACD 320871) were used to subtract background signals beforehand. The macro for assessing signal thresholds is available from GitHub (data and code availability). Step-by-step protocol is available on the ACD Bio webpage (https://acdbio.com/rnascope-multiplex-fluorescent-v2-assay).

### Flow cytometry staining and acquisition

After dissection and digestion, cells were filtered through 40 μm cell strainers (Falcon), followed by washing and centrifugation for 5 min at 250 g at 4°C. For flow cytometric analysis, cells were resuspended in 20 μl PBS plus Viability Dye eF506 (eBioscience, conc. 1:500) and incubated for 10 min at RT in the dark. Proceeding with cell staining, 100 μl PBS plus 2% FCS with corresponding antibodies (see key resources table) was added and cells were incubated for 30 min at 4°C in the dark. Post staining, cells were washed again and analyzed using the BD LSR II cytometer according to manufacturer's instructions and marker combinations and gating strategies. FAC sorting as preparation for single-cell transcriptional analysis was performed on the FACSAria II from BD Biosciences using an 85μm nozzle. Gating of live cells was achieved by exclusion of PI-high cells. Doublets were excluded by plotting SSC width versus SSC area. Approximately 70.000 cells were collected in sorting media (containing 0.04% BSA and 1mM EDTA in PBS) in 1.5 ml Eppendorf tubes, chilled on ice, and immediately processed for single-cell transcriptional analysis. Step-by-step protocol (MIFlowCyt protocol) is available in Biostudies (see key resources table).

### Generation of single cell transcriptomes

Mouse reproductive tissues and spleen were enzymatically dissociated and FAC sorted, and the undiluted single-cell suspension at a concentration of 467 cells/μl was loaded per channel of either the ChromiumTM Single Cell B or G Chip (10X Genomics® Chromium Single Cell 3' Reagent Kits v3.0 and Chromium Next GEM Single Cell 3' Reagents Kits v3.1, respectively), aiming for a recovery of 5,000 cells. On Chromium Next GEM Chip, Gel Beads-in-emulsion (GEMs) were formed by combining barcoded Gel Beads, a Master Mix containing cells, and Partitioning Oil. Reverse transcription performed in GEMs produced barcoded, full-length cDNA from poly-adenylated mRNA. Following purification of the cDNA from the reverse transcription reaction mixture, cDNA was amplified for 11 cycles using a thermal cycler (C1000 Touch, Bio-Rad). Indexed libraries were finally constructed via End Repair, A-tailing, Adaptor Ligation, and amplified by PCR. Libraries were prepared using Single Index Kit T Set A (10X Genomics) for indexing. Libraries were sequenced on Illumina NovaSeq 6000 using a paired-end run sequencing with 26 bp length on read 1 and 98 bp on read 2. Step-by-step protocol is available on the 10x Genomics support web-page (https://www.10xgenomics.com/support).

### Spatial transcriptomics

Three month old *Mus musculus* (C57Bl6/J) female mice were sacrificed at diestrus together with 18 month old mice. No sample size estimation was performed. Ovaries and uteruses were dissected and embedded into an optimum cutting temperature matrix (O.C.T., Tissue Tek) using a bath of pre-cooled (-60-70°C) isopentane (Sigma) on dry ice. Blocks were cut using cryo-microtome (CM3050S, Leica), head temperature set at -10°C. 10 μm thick tissue slices were placed on Visium Spatial Gene Expression Slides (10X Genomics) and stained with Hematoxylin and Eosin (H&E). For ovaries staining time in hematoxylin was 5 min, 30 s in blueing agent, and 1 min in eosin; for uteruses 7 min in hematoxylin, 30 s in blueing agent and 2 minutes in eosin. To release mRNA from the cells, tissues were permeabilized. Optimal permeabilization time for ovarian and uterine tissues was 18 and 24 minutes, respectively. Reverse transcription was performed on poly-adenylated mRNA captured on the slide. Spatially barcoded, full-length cDNA was amplified using a thermal cycler (C1000 Touch, Bio-Rad). Libraries were prepared using Dual Index Kit TT Set A (10X Genomics) for indexing. Samples were sequenced on NovaSeq6000 using a paired-end run sequencing with 28 bp length on read 1 and 91 bp on read 2. Step-by-step protocol is available on the 10x Genomics support web-page (https://www.10xgenomics.com/support).

### Filtering and normalization of scRNA-seq data

Raw sequencing reads were processed using Cellranger analysis pipeline (v 3.0.1). The "cellranger count" command was used to generate filtered and raw matrices. Reads were aligned against the mouse genome version mm10 (Ensembl release 93). Filtered gene-barcode count matrices were further analyzed using the R package Seurat v 4.0.5.[75]

To remove low quality cells, an adaptive filtering threshold approach was used based on high mitochondrial RNA content, extreme numbers of counts (count depth), and extreme numbers of genes per barcode. Cells were filtered based on the median absolute deviation (MAD) from the median value of each metric across all cells. Specifically, we considered a value as an outlier when differing by more than 3 MADs from the median. The filtering step was performed using the R package Scater v 1.16.2.[76] Counts were normalized using the ScTransform normalization approach of Seurat. Cell cycle gene effect was regressed out using the CellCycleScoring function in Seurat. All clusters in all samples showed consistently low doublet scores using doubletCluster and doubletCells of R package Scran v 1.16.0.[77]

### Cell type annotation of scRNA-seq data

Each organ was processed independently for cell type annotation. Organ-specific UMAPs were constructed using a subset of features (genes) exhibiting high cell-to-cell variation which were identified by modeling the mean-variance relationship. The top 2000 features were used to perform PCA analysis. To cluster the cells, a K-nearest neighbor (kNN) graph based on the euclidean distance in PCA space was first constructed using the first 30 PC components as input. Next, the Louvain algorithm was applied to iteratively group cells. We identified the cell types in each cluster using a combination of manual and automated approaches from known marker genes. First, clusters were assigned to known cell populations using cell type–specific markers obtained through the FindAllMarkers function. Multiple testing correction was performed using Benjamini-Hochberg procedure. Second, the R package Garnett v 0.1.20[78] in cluster extension mode was used to annotate cells in a semi-automated manner. Because some clusters remained unclassified by either the manual or semi-automated approach - or in rare cases were differently classified by the two approaches - a Support vector Machine with rejection ($SVM_{rej}$) was applied as an additional automated classifier. Cluster annotations in agreement between the manual and automated approach were used as the training set for the $SVM_{rej}$. The e1071 library[79] (v 1.7-13) was used to implement the $SVM_{rej}$ classifier. Classification was performed using a linear kernel with the cost function set to 10. Rejection rates of 10% and 30% were used to classify level 1 and level 2 annotations, respectively. Cell clusters of 18 month old and pregnant mice were annotated using an $SVM_{rej}$ classifier trained on cell clusters of normally cycling young mice.

## Batch correction of scRNA-seq data

Cells from multiple organs in the estrous cycle were integrated together for visualization purposes. Integration and batch correction of samples of young cycling mice was performed using the Reciprocal PCA together with "LogNormalize" normalization method from Seurat. For each organ, in order to remove batch effects we chose the sample with the highest number of cells (regardless of its cycle phase) to anchor pairwise comparisons. Integration of young (diestrus) and old mice followed a similar approach.

Integration of samples of pregnant mice with metestrus samples was performed separately using Canonical correlation analysis together with SCT normalization (Seurat). Batch corrected data was used only for UMAP visualization purposes; all other downstream analyses including differential expression were performed on uncorrected data. To improve the visualization of gene expression in UMAP plots, we used a kNN-pooling approach.[80] A kNN graph was constructed based on euclidean distance in PCA space, and cell counts were pooled across 50 nearest neighbor cells, thus decreasing technical noise in scRNA-seq caused by dropout events.

## Inter-quartile range calculation

Cell proportions for each cell type in each biological replicate were calculated and averaged per estrous phase. These averages were then used to calculate the interquartile range for each cell type. To display the uncertainty, the cell proportions for each cell type in each biological replicate were calculated. All possible combinations of one replicate mouse per estrous phase were listed and all possible interquartile ranges were calculated.

## Differential cell abundance analysis

To assess if the proportions of cell populations in individual organs change along the estrous cycle and in aging, a compositional regression model was used. Cell population compositions were used as dependent variables, and estrous cycle phases or age as independent variables. Estrous cycle phases were compared in a pair-wise manner. Components of the compositions were amalgamated and expressed as compositions of two components due to low number of replicates. Prior to model fitting, composition components were transformed using isometric Log-Ratio Transformation. The R package Compositions[81] (v 2.0-4) was used to perform the Log-Ratio transformation and compositional regression. Innate vs adaptive immune cells ratio was calculated as ratio of number of innate immune cells (N, DC, M1Mp, M2Mp, Mp and MaC) and number of adaptive immune cells (NKC, BC, iNkT, MAIT, MTC) in each individual.

## Optimal transport

Balanced optimal transport (OT) analysis was performed to assess the magnitude of transcriptional changes between cell populations of all organs in different phases of the estrous cycle, as well as between old and young (diestrus) cell populations. For specific subgroups of samples, we performed simultaneous NMF embeddings; these two subgroups included all organs of all estrous phases and all organs of young (diestrus) together with all organs of old mice. NMF embeddings were calculated on the set of top 2000 most highly-variable genes using the Block Principal Pivoting method of the PLANC library (v 0.81).[92] Rank 10 of NMF embeddings, chosen based on decrease in cophenetic coefficient,[100] was used for OT distance calculation. OT distances were calculated for all cell populations which contained at least 100 cells in any of the compared groups. As the balanced optimal transport problem is constrained with a mass balance condition, the OT distance between two cell populations was calculated as an average of 100 random samples of 100 cells in a stochastic sampling approach. We tested different sample sizes using simulated data and determined that sampling 100 cells can accurately quantify differences in gene expression distributions. The OT distance was defined as a minimum-cost flow solution problem and was solved using Munkres algorithm.[57]

## Differential gene expression (DGE) analysis

DGE analysis was performed using a mixed generalized negative binomial regression model with random intercept. Normalized gene counts were used as the dependent variable, while estrous cycle phases or age were used as the independent variable, and sample label as random effect. Model was fitted gene-wise for each cell subpopulation. Estrous cycle phases were compared in a pair-wise manner. The model fitting was performed using the glm.nb function of lme4 R package[82] (v 1.1-27.1). Only genes that were expressed across 10 cells with at least 1 count were used in model fitting. If the model fitting showed singular fit (indicating overfitting) the p-value was set to *NA*. P-values were corrected for multiple testing using Benjamini-Hochberg procedure. All genes with padj value smaller than 0.05 were considered differentially expressed.

## Overrepresentation analysis (ORA)

A hypergeometric test was used to perform ORA analysis. Gene sets used in ORA analysis are part of the MsigDB[91] (https://www.gsea-msigdb.org/gsea/msigdb/, v 7.2) pathway collection (H; C2: Kegg, Reactome; and C5: GO Biological Process). For the ORA in Figure 2, we used MSigDB H and Reactome, and excluded pathways with the term "Disease" in their descriptor. Multiple testing correction was performed using the Benjamini-Hochberg procedure. All pathways with an adjusted p-value < 0.1 in at least one organ are shown.

## Scoring of gene set activity in single-cell RNA-seq data

Scoring of gene set activity was performed using the AUCell R package v.1.10.0.[95] AUCell was used to assess if certain gene sets were enriched within the top 5% or 10% expressed genes for each cell. Gene sets used in the analysis are the same as gene sets used in ORA. To score the activity of inflammatory and ECM genes pathway HALLMARK_INFLAMMATORY_RESPONSE and REACTOME_EXTRACELLULAR_MATRIX _ORGANIZATION were used, respectively. HALLMARK_INFLAMMATORY_RESPONSE is a manually curated gene set containing 200 genes that define inflammation, 40 of which are cytokines and growth factors, and 41 of which are cell differentiation markers.[91] Moreover, the gene set contains 37 genes previously shown to be upregulated in fibroblasts with a pro-inflammatory phenotype that is common across 4 chronic-inflammatory diseases in both human and mouse.[101] For the scoring of the activity of target genes of each ligand in fibroblasts, we used the NicheNet (v 1.1.1) ligand-target model to obtain a list of predicted targets for each ligand.[39] AUCell scores were calculated for each cell and averaged across conditions for each cell population. Average scores across the cycle were weighted to account for the different phase lengths (the cycle was roughly estimated to be partitioned 60% diestrus and the remainder equally divided between proestrus, estrus and metestrus.[98] A mixed generalized linear regression model with random intercept was used to test the significance of the activity score changes across the estrous cycle. Activity scores were used as the dependent variable, while estrous cycle phases were used as the independent variable, and sample label as random effect. Model was fitted under beta distribution using the glmmTMB package (v 1.1.5). P-values were corrected for multiple testing using Benjamini-Hochberg procedure.

## DGE analysis using Mutual-information (MI)

The human endometrium dataset was retrieved from NCBI's Gene Expression Omnibus (accession code GEO: GSE111976). Raw count matrices of Fluidigm C1 dataset were normalized using the ScTransform normalization approach. Cycle phase labels of human samples were assigned based on the original publication's metadata.[13] Dependence of gene expression and cycle phase label in fibroblasts and decidual cells was calculated as the MI between these two variables, as described in [13]. The same calculation was performed for the human fibroblasts. Briefly, for each gene, MI was calculated using the Java implementation of ARACNe-AP (v 1.0).[94] The statistical significance of MI was evaluated using the permutation approach, in which MI value for each gene was compared to a null distribution obtained by permuting cycle phase labels 1,000 times. Multiple testing correction was performed using Benjamini-Hochberg. As the mouse dataset was substantially bigger than the human dataset, MI and its associated p-value for the mouse dataset were calculated on 100 random samples of 2000 cells in a stochastic sampling approach. P-values associated with genes in all mouse random samples were aggregated using Fisher's method (R package aggregation, v 1.0.1). Genes associated with padj value smaller than 0.05 were considered as cycle-associated genes in mouse and human. We identified the set of conserved transcriptional changes between human and mouse cycles by identifying homologous cycle-associated genes that showed the same directionality of regulation in comparison to adjacent cycle phases in paired mouse-human cycle phases. For instance, a mouse gene upregulated in proestrus compared to diestrus and the homologous human gene upregulated in proliferative early compared to secretory late. Genes that showed opposite directionality of regulation (e.g. up-regulation in humans, down-regulation in mice) were considered divergent. Mouse and human cycle phases were paired based on ovulation timing and uterine cycle events (proliferation vs secretion).[102,103] Proestrus was paired with proliferative early phase, estrus with proliferative late, metestrus with secretory early, decidualization with secretory mid and diestrus with secretory late. Cells of menstruation phase in humans could not be paired with normally cycling mouse cells and were excluded from this analysis. To calculate the proportion of the conserved genes expected by chance in each cycle phase, labels of upregulated, downregulated and neutral (not up- or down- regulated) genes of all homologs in mouse and human for corresponding cycle phases were permuted 100 times and proportions of the conserved/divergent genes were calculated per cycle phase. Final value of conserved genes proportion was calculated as an average of proportion of conserved downregulated and upregulated genes in all permutations runs.

## Cell-to-cell communication analysis

To assess cellular communication from different cell types to fibroblasts, we used a multiplication of expression between receptors and ligands (expression product) as a communication score. The list of mouse ligand-receptor pairs that was used in the analysis was extracted from CellChat[96] and CelltalkDB repositories.[97] To compare cellular crosstalk among the different organs, we first focused on the average expression values of ligands in all cell types and receptors in fibroblasts, regardless of the source of the ligand. To calculate the communication score, averaged ligand expression counts in all cells from all cycle phases were multiplied with averaged receptor counts in fibroblasts. For multi-subunit receptors, the subunit with the minimum average expression was used in our calculations as previously proposed.[104] This analysis was performed in each reproductive tissue.

The statistical significance of the difference of expression product in all reproductive organs was evaluated using a permutation approach. All pairwise combinations of log ratios of expression product in all organs for each ligand-receptor pair were compared to null distribution obtained by permuting the organ labels 1000 times. A similar approach was used to evaluate the statistical significance of the difference of expression product upon aging. For each organ, log ratios of expression product of old and young fibroblasts in diestrus were compared to a null distribution obtained by permuting the age labels 1000 times. Multiple testing correction was performed using the Benjamini-Hochberg procedure. This analysis does not take into account the spatial distribution of the cells.

For selected ligand-receptor pairs, we then determined which cell types were the likely sources of the ligand. The total sum of ligand counts for each cell type was calculated, thus taking into consideration the cell abundance and average expression of ligand in each cell type. These sums were subsequently transformed into z-scores across cell types. We chose to closely analyze the ligand-receptor pairs related to inflammation and ECM, based on the known role of receptor-ligand interactions in shaping their functions.[105–107]

## Spatial transcriptomics analysis

The raw reads were processed using spaceranger (10X Genomics, v 1.3.1). To deconvolute the spatial data and estimate gene expression for every cell type inside every spot DestVI v.1.0.3 was used together with corresponding tissue single-cell reference [84]. Cell proportions calculated for each spot were thresholded using an automatic thresholding strategy implemented in the DestVI utilities package (v 0.1). Lower cell proportions thresholds were inspected and manually adjusted according to tissue architecture inferred from histology images of the slides, as recommended by the developers of DestVI. For example, luteal cells are expected to be exclusively located in the corpus luteum. DestVi automatically detected high proportions of luteal cells in the corpus luteum and low proportions outside of the corpus luteum. To optimize this, the lower threshold for detection of luteal cells was adjusted in a way that ignores background values of luteal cells in the stroma. Detection thresholds, cell proportions and imputation reads are available through Biostudies (see data and code availability).

To explore the spatial niches of inflamed stromal cells in young uteruses and ovaries, a mixed linear generalized model with random intercept was used. In the uterus stromal cells are fibroblasts, in the ovary stromal cells are theca cells and fibroblasts. Theca cells and fibroblasts have very similar transcriptional profiles so it was not possible to train DestVI to successfully distinguish between them. Inflammation activity scores calculated using AUCell were used as the dependent variable, while the proportion of different cell types in the neighborhood or their inflammation score were used as the independent variable, and sample label as random effect. Model was fitted using lme4 package (v 1.1-27.1). To determine the proportion of the variance explained for the dependent variable marginal R squared values were calculated using the MuMIn package[85] (v 1.47.5).

To test if highly inflamed stromal cells cluster together cluster coefficients were calculated. First, inflammation activity scores for each stromal cell (SC) spot in each ovary and uterus were calculated using AUCell. SC spots are defined as spots with a minimum estimated proportion of stromal cells (as estimated by DestVI). Using DestVI, we performed cell-type specific imputation of gene expression across all spots. Imputed values represent the average gene expression of all cells of specific cell type on each spot. Imputed values of SC cells were used as input for AUCell. We considered only sections of ovaries and uterus which had at least 20 and 50 spatially connected stromal cells, respectively. Spatially connected stromal cells are defined as spatially connected spots with a minimum estimated proportion of stromal cells. Different thresholds for two tissues were chosen based on differences in their tissue architecture. Ovary has a large number of different structures interspersed in the stroma, such as follicle and corpora luteum/albicans, while stroma in the uterus tends to be in a more continuous layer. Therefore the threshold for the ovary was lowered in comparison to the uterus. Next, inflammation scores in these sections were binarized by assigning the high inflammation label to the top 25% spot with the highest score. Finally, spatial graphs of SC spots with high inflammation labels were constructed by connecting spots which are direct neighbors and their global cluster coefficients (type set to "average") were calculated using iGraph package (v 1.5.0).

The cell-to-cell communication analysis based on spatial data was used to confirm and expand the initial scRNA-seq analysis. The cell-to-cell communication analysis was performed by calculating a ligand-receptor interaction score in each neighborhood. For each spot, the neighborhood refers to the combination of the spot itself and the directly adjacent spots. We assume that ligand molecules can diffuse freely throughout the neighborhood. To calculate the amount of available ligand in each spot, the ligand expression in all cell types was averaged across all the spots in the neighborhood. An interaction score was then computed for each ligand-receptor pair in the database (see cell-to-cell communication analysis) by multiplying the available ligand expression in the spot by the receptor expression in fibroblasts. This score was weighted by the proportion of signal captured by fibroblasts.

To compute the proportion of signal captured by each cell-type, we calculated the proportion of receptor expressed in that cell-type inside each neighborhood, and averaged across all neighborhoods.

## Single-Cell Regulatory Network analysis

pySCENIC (v 0.12.1) was used to perform single-cell regulatory network analysis in fibroblasts[86] by using SCT normalized gene expression values of specific subsets of cells, i.e. fibroblasts of all organs in all phases of the cycle, fibroblast of all organs in diestrus and aged samples, and uterine fibroblasts in metestrus and pregnant samples. The gene co-expression networks were determined using grnboost2, enriched transcription factor motifs were predicted using ctx function and regulon activity scores were calculated using AUCell. To assess if regulons are differentially active across FRT organs or in aging, the activity score for each regulon was compared to null distributions obtained by permuting organ- or age-labels 1000 times. Multiple testing correction was performed using Benjamini-Hochberg procedure.

Selection of the subset of transcription factors related to inflammation and ECM was based on the overlap and enrichment of transcription factor target genes and target genes of selected ligands obtained from the NicheNet database. Additionally, classification of transcription factors as fibrosis and/or inflammation associated was based on the enrichment score of transcription factor target genes in inflammation (Hallmark collection) and ECM organization (Reactome collection) pathways. Transcription factor target genes were identified in pySCENIC analysis. Jaccard index was used to quantify overlap between target genes and pathway related genes, and a hypergeometric test was used to assess the enrichment.

### Single-cell trajectory inference

Slingshot (v 1.6.1) was used to infer fibroblast trajectories along the estrous cycle.[87] Linear discriminant analysis (LDA) was used to perform dimensionality reduction. LDA was performed on cycle-associated genes determined in MI approach using the mda R package[88] (v 0.5–3). We clustered the cells using k-Means, and we fitted the principal curve through fibroblast clusters using the Slingshot function.

### Transcriptional heterogeneity analysis

Differential Shannon Entropy (ShE) was used to assess the differences in transcriptional heterogeneity between young (diestrus) and old cell populations. Differential ShE was calculated using the EntropyExplorer package (v 1.1).[89] Multiple testing correction was performed using the Benjamini-Hochberg procedure. To exclude that differential Shannon entropy is confounded with mean expression, we plotted the mean difference against differential Shannon entropy for all genes in fibroblasts in the ovary. We conclude that the difference in Shannon entropy is not driven by differences in means between young and old.

### Linear mixed models of inflammation

To estimate the rate of inflammaging in the different organs, we fit a linear mixed model at the cell level including age, organ and the interaction of age and organ as fixed effects, and individual (mouse) as a varying intercept random effect.

## QUANTIFICATION AND STATISTICAL ANALYSIS

Statistical analysis and R/python packages used to perform it are described for each bioinformatics analysis in the corresponding section of the Method details section. Exact value of biological replicates/animals (n) can be found in the figure legends and results section. Number of biological replicates for scRNA-seq and spatial transcriptomics experiments is listed in Figure 1A. For all other experiments this number is listed in the figure legend which describes the result of the experiment. Statistical significance was defined as p-value or p-value adjusted smaller than 0.05. Functions descdist and fitdist of R package fitdistrplus[90] (v 1.1-11) were used to assess the underlying data distributions.

## ADDITIONAL RESOURCES

Dynamics of cellular abundance, gene expression, cell-to-cell communication and transcription factor regulatory networks in FRT organs in estrous cycle, decidualization and aging, can be explored through our interactive tool at https://cancerevolution.dkfz.de/estrus/.

# Supplemental figures

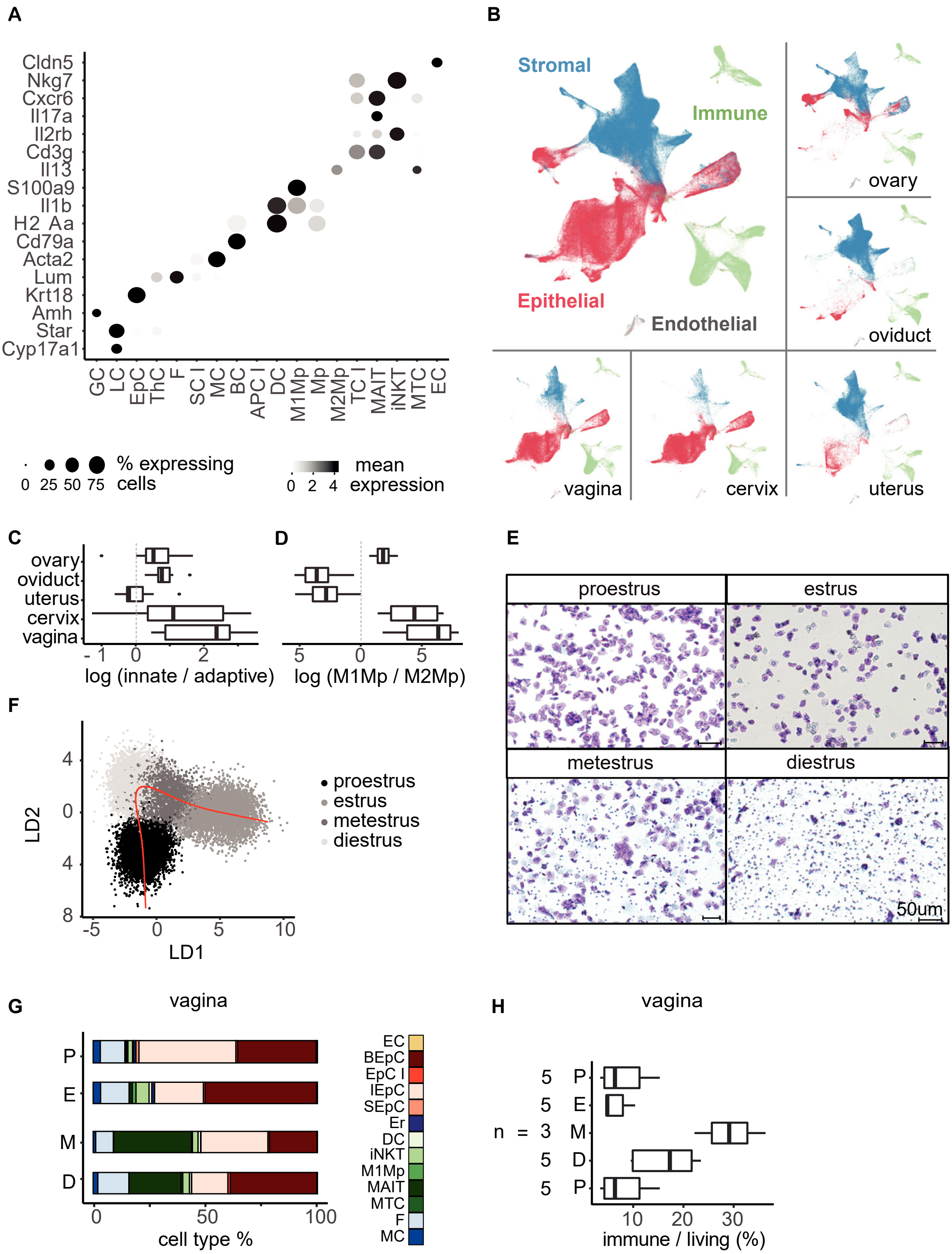

(legend on next page)

**Figure S1. Single-cell characterization of the female reproductive tract, related to Figure 1**

(A) Selected marker genes used to classify ovarian cell types. Full plots of marker genes used to classify all FRT organs are available in Biostudies (see Data and code availability).

(B) UMAP plot of the young cycling mouse cells. Cell types were assigned to epithelial (red), immune (green), stroma (blue), and endothelial (gray) compartments. Organ subpanels show the same UMAP embedding as the central figure, but restricted to cells originating from each organ.

(C) Ln ratio of innate (N, DC, M1Mp, M2Mp, Mp, and MaC) and adaptive (NKC, BC, iNkT, MAIT, MTC) immune cells' abundances in FRT organs. Each data point represents a biological replicate.

(D) Ln ratio of M1 to M2 macrophages in FRT organs. Each data point represents a biological replicate.

(E) Crystal violet staining of vaginal smears of young cycling mice. Cycle phases (proestrus, estrus, metestrus, and diestrus) were assigned based on occurrence of leukocytes and nucleated and cornified epithelial cells.

(F) Pseudotime-time trajectory of uterine fibroblasts across the cycle. Cell clusters are colored according to cycle phases. Dimensionality reduction was performed using linear discriminant analysis (LDA) and cell features projected to the first two linear discriminant (LD) components were plotted.

(G) The average % across biological replicates of each cell type in the vagina at each phase of the cycle. Barplots showing for each cell type and its composition across the biological replicates are shown in Figure S2A. Statistical significance of cell abundance proportion changes across estrous cycle is listed in Table S3.

(H) The cyclical changes in the vaginal immune compartment assessed using flow cytometry ("n," number of biological replicates).

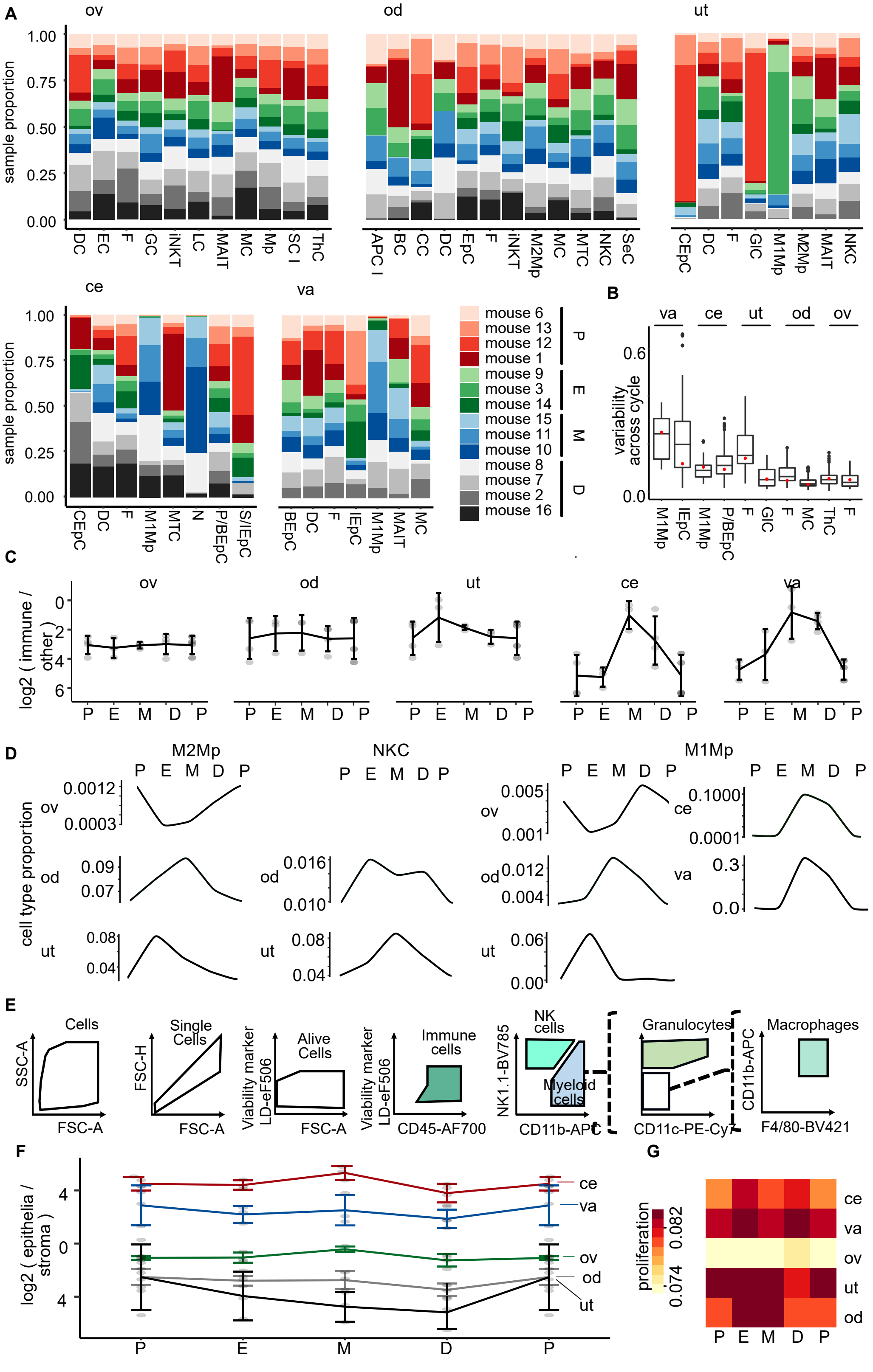

*(legend on next page)*

**Figure S2. Changes in cell-type abundances in FRT tissues across the estrous cycle, related to Figure 1**

(A) Barplots showing for each cell type and its composition across the biological replicates. Cell types that exceed at least 1% of total cells in each tissue are shown. Statistical significance of cell abundance proportion changes across estrous cycle is listed in Table S3.

(B) Uncertainty of interquartile ranges of cell-type proportions for each phase of the cycle, calculated as all possible combinations of one replicate mouse per estrous phase. Red dot indicates interquartile range of cell-type proportions averaged over biological replicates, which is plotted in Figure 1C. Plots showing the uncertainty of the interquartile ranges for all cell types are available through Biostudies (see Data and code availability).

(C) The ratio of immune to other cells for each biological replicate is plotted. The ratios are shown together with their standard errors.

(D) Compositional changes of M2Mp, NK, and M1Mp cells across the cycle in all FRT organs.

(E) Fluorescence-activated cell sorting (FACS) gating strategy used to quantify immune cells in vaginal and uterine samples across the cycle.

(F) The ratio of epithelia to stroma for each biological replicate is plotted. The ratios are shown together with their standard errors.

(G) Average activity score of genes promoting cell proliferation (GO:0008284) calculated in stromal cells using AUCell. p values indicating significance of pathway activity scores between estrous cycle phase are listed in Table S7.

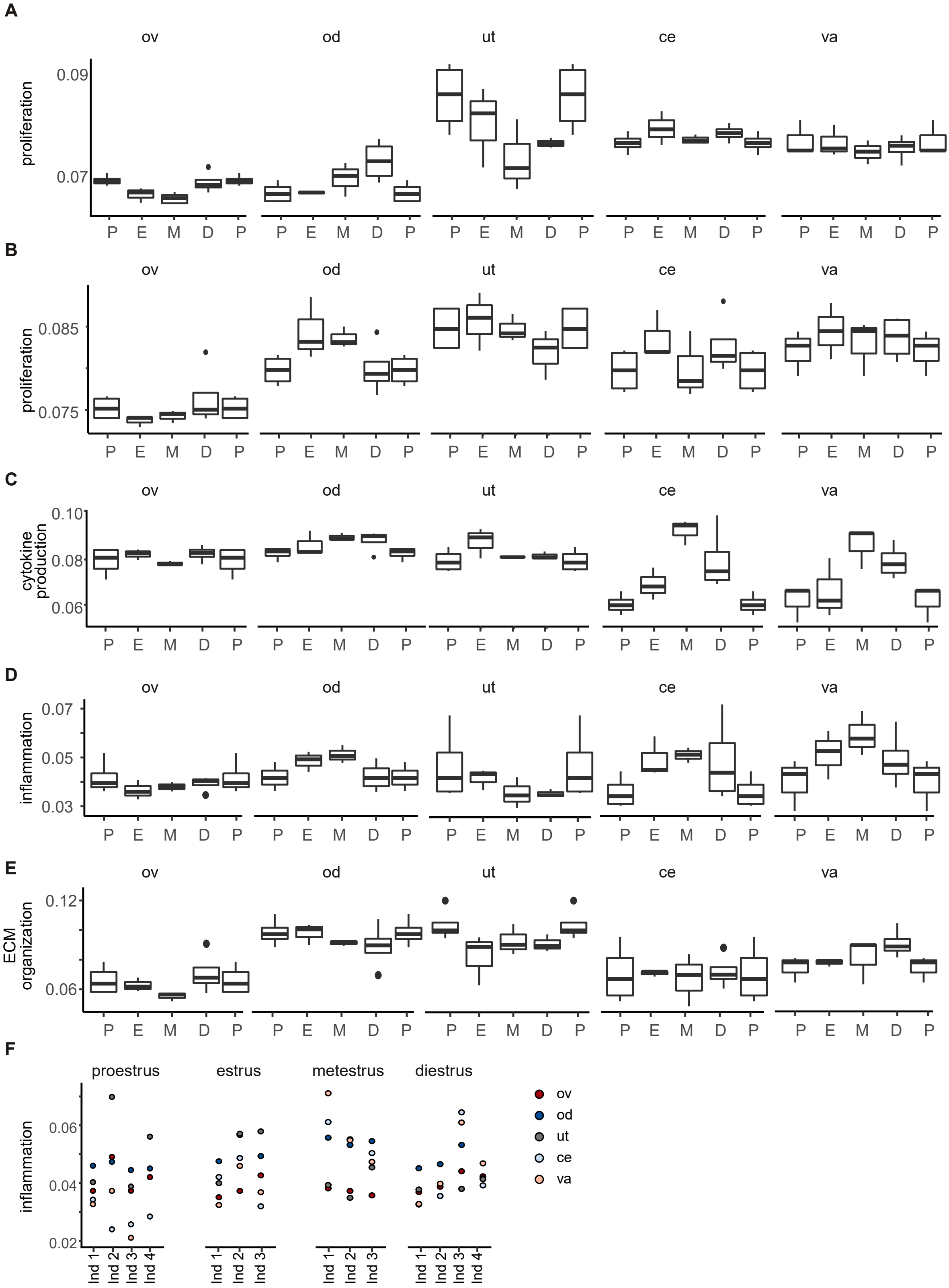

*(legend on next page)*

**Figure S3. Distribution of activity score of pathways relevant to FRT function, related to Figures 1 and 2**

(A) Distribution of activity score of genes promoting cell proliferation (GO:0008284), calculated in epithelial cells using AUCell.
(B) Distribution of activity score of genes promoting cell proliferation (GO:0008284), calculated in stromal cells using AUCell.
(C) Distribution of activity score of cytokine regulatory genes (GO:0001816), calculated in immune cells using AUCell.
(D) Distribution of activity score of inflammatory genes calculated in fibroblast using AUCell.
(E) Distribution of activity score of ECM organizational genes calculated in fibroblast using AUCell.
(F) Average activity score of inflammatory genes calculated in fibroblasts of separate FRT organs per individual.

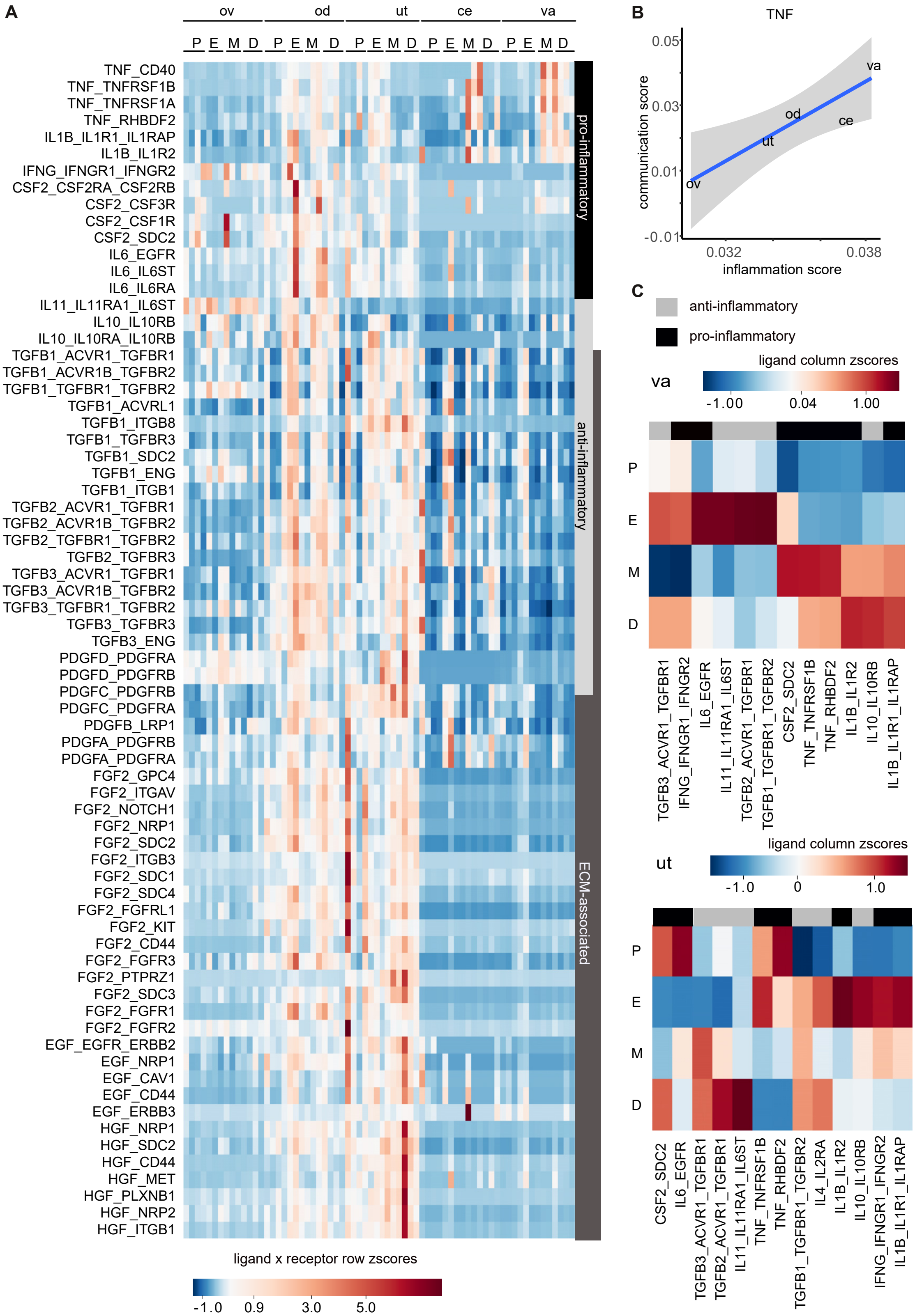

*(legend on next page)*

**Figure S4. Inflammation- and ECM-related cell-to-cell communication scores in FRT tissues across the estrous cycle, related to Figures 1 and 2**

(A) Heatmap showing the *Z* scores of ligand-receptor products in each individual. Ligand expression is averaged across all cell types; receptors are in fibroblasts only.

(B) Scatterplot showing correlation between expression product of TNF::TNFRSF1B and the activity score of predicted targets of the Tnf ligand.

(C) Heatmap showing the *Z* scores of inflammatory ligand-receptor products in the vagina and uterus across cycle phases. Ligand expression is averaged across all cell types; receptors are in fibroblasts only.

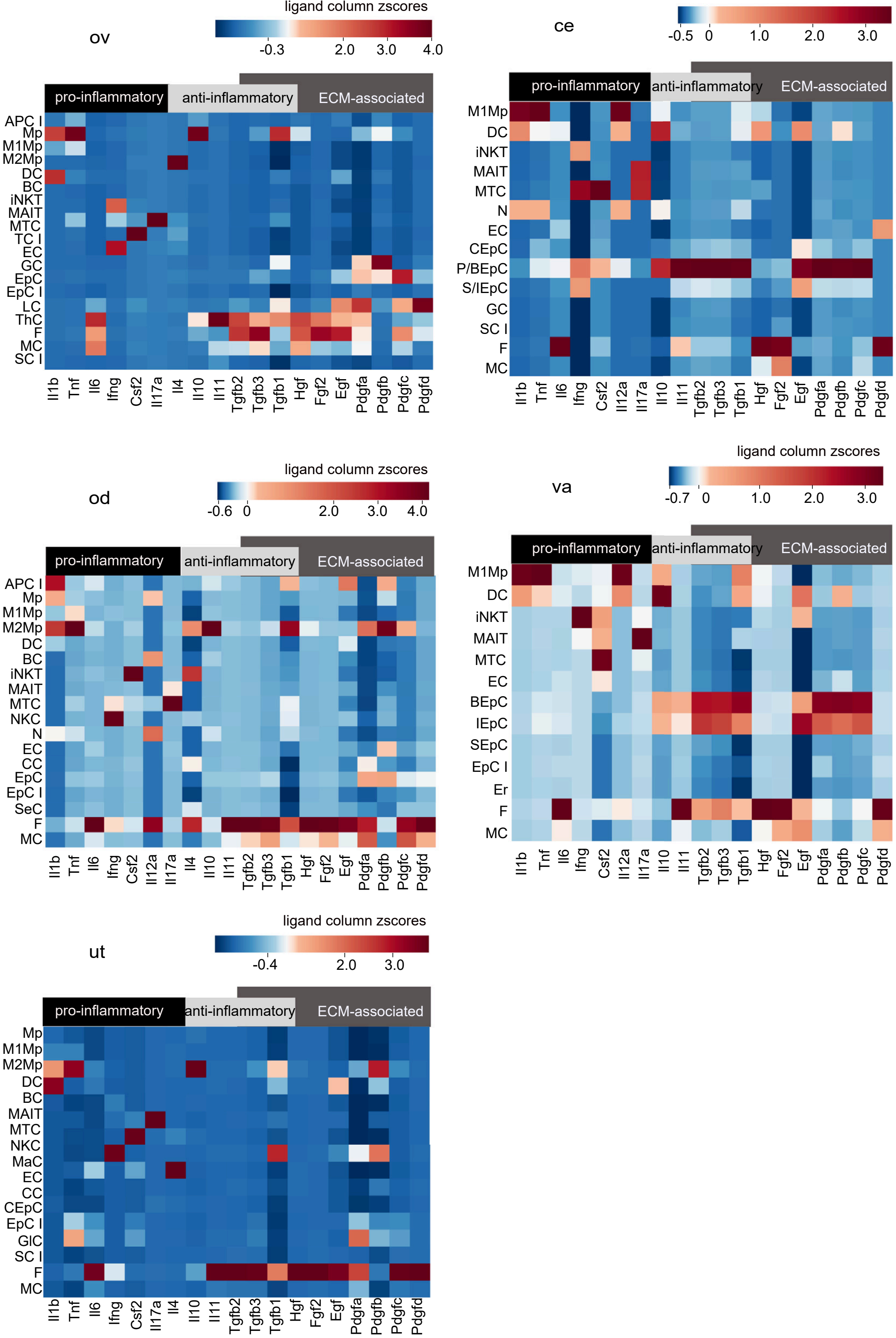

**Figure S5. Ligand expression in all cell types of ovary, oviduct, uterus, cervix, and vagina, related to Figure 2**

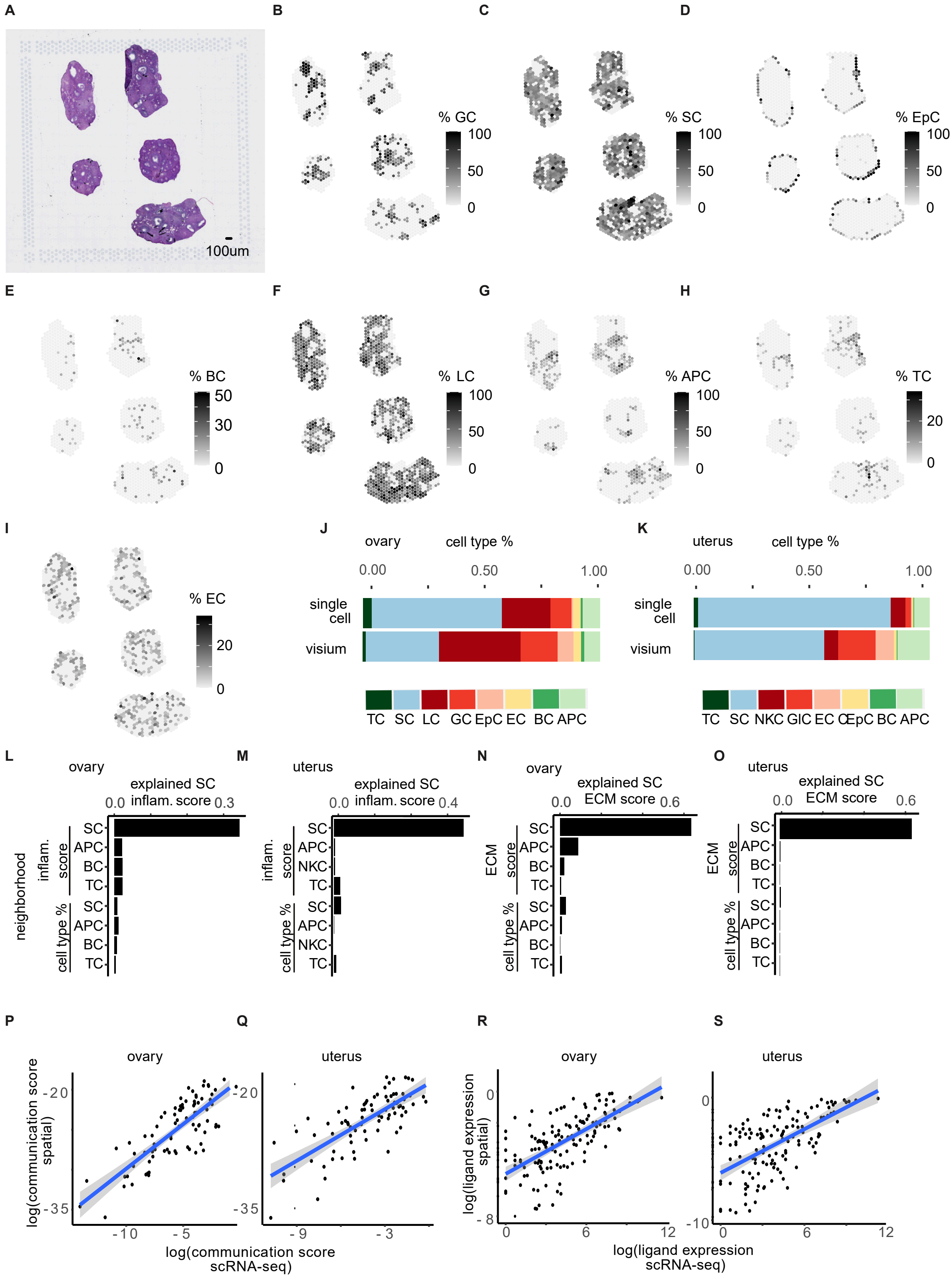

*(legend on next page)*

**Figure S6. Spatial transcriptomics characterization of the FRT, related to Figure 3**

(A) H&E staining of young ovary.

(B–I) Proportion of granulosa cells (GCs) (B), stromal cells (SCs) (C), epithelial cells (EpCs) (D), B cells (BCs) (E), luteal cells (LCs) (F), antigen-presenting cells (APCs) (G), T cells (TCs) (H), and endothelial cells (ECs) (I) per spot in the young ovary shown in (A).

(J and K) Barplots showing % of each cell type in the ovary (J) and uterus (K) in single-cell RNA-seq and Visium slides V11M25-311_B1 and V12N14-363_B1.

(L and M) Proportion of SC inflammation scores in the ovary (L) and uterus (M), explained by inflammation scores of cell types in the neighborhood or by their proportions.

(N and O) Proportion of SC ECM scores in the ovary (N) and uterus (O), explained by ECM scores of cell types in the neighborhood or by their proportions.

(P and Q) Agreement between communication scores calculated in scRNA-seq and spatial-transcriptomics-based analysis of the ovary (P) and uterus (Q).

(R and S) Agreement between ligand expression, calculated in scRNA-seq and spatial-transcriptomics-based analysis of the ovary (R) and uterus (S).

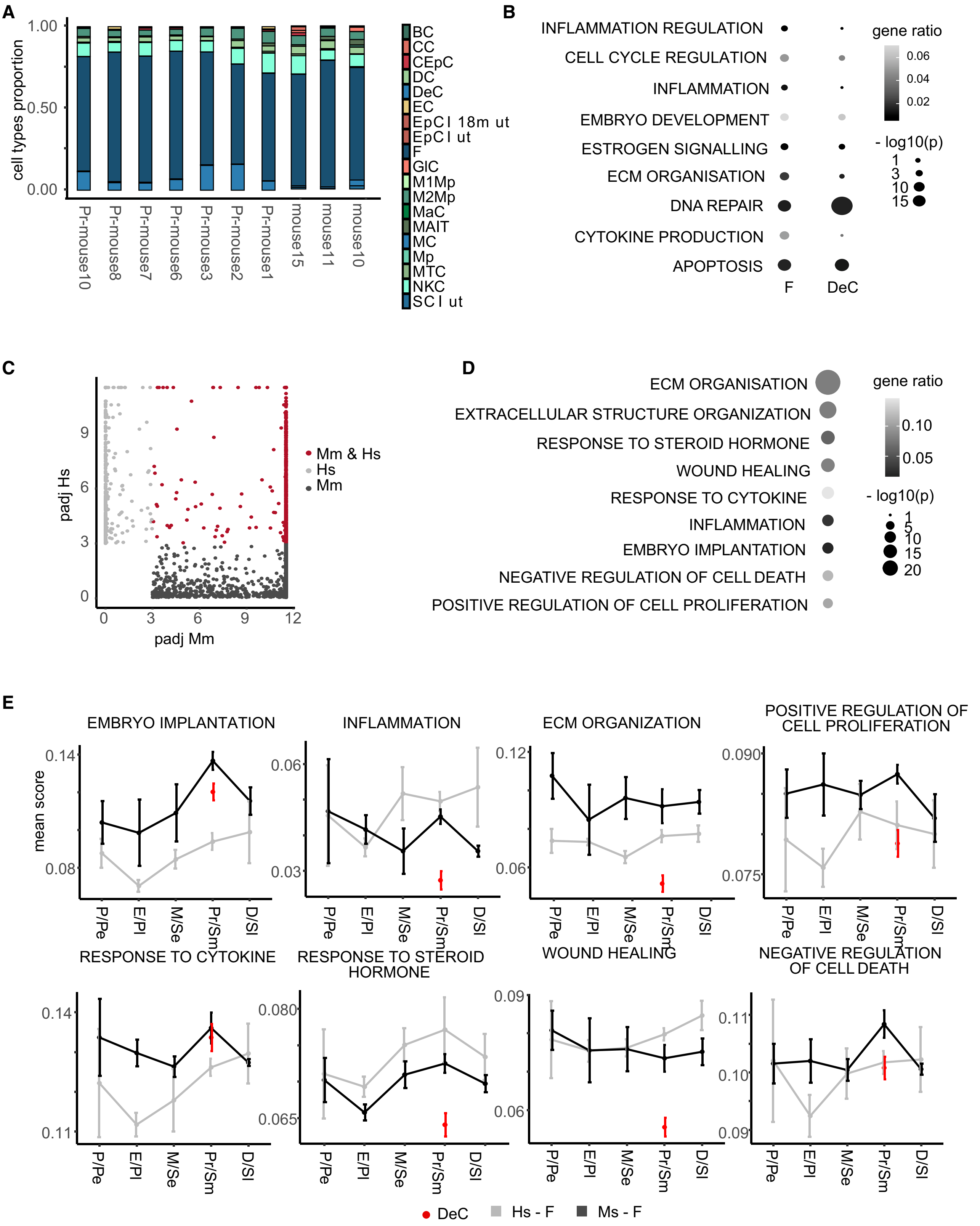

(legend on next page)

**Figure S7. Single-cell characterization of the decidualized FRT, related to Figure 4**

(A) Barplots showing % of each cell type in the uterus in metestrus and in pregnancy in each biological replicate.

(B) Over-representation analysis of differentially expressed genes between metestrus and pregnant mice in fibroblasts and decidual cells using mixed linear model (STAR Methods).

(C) Scatterplot of adjusted p values of mouse and human homologous, differentially expressed genes across the cycles, calculated using the MI approach.

(D) ORA analysis of differentially regulated genes that intersected in mouse and human cycles, identified using MI approach (STAR Methods).

(E) Activity scores of genes in overrepresented pathways (B) determined by AUCell and averaged across all mouse or human fibroblasts and mouse decidual cells in paired cycle phases. The average scores are shown together with their standard deviations.

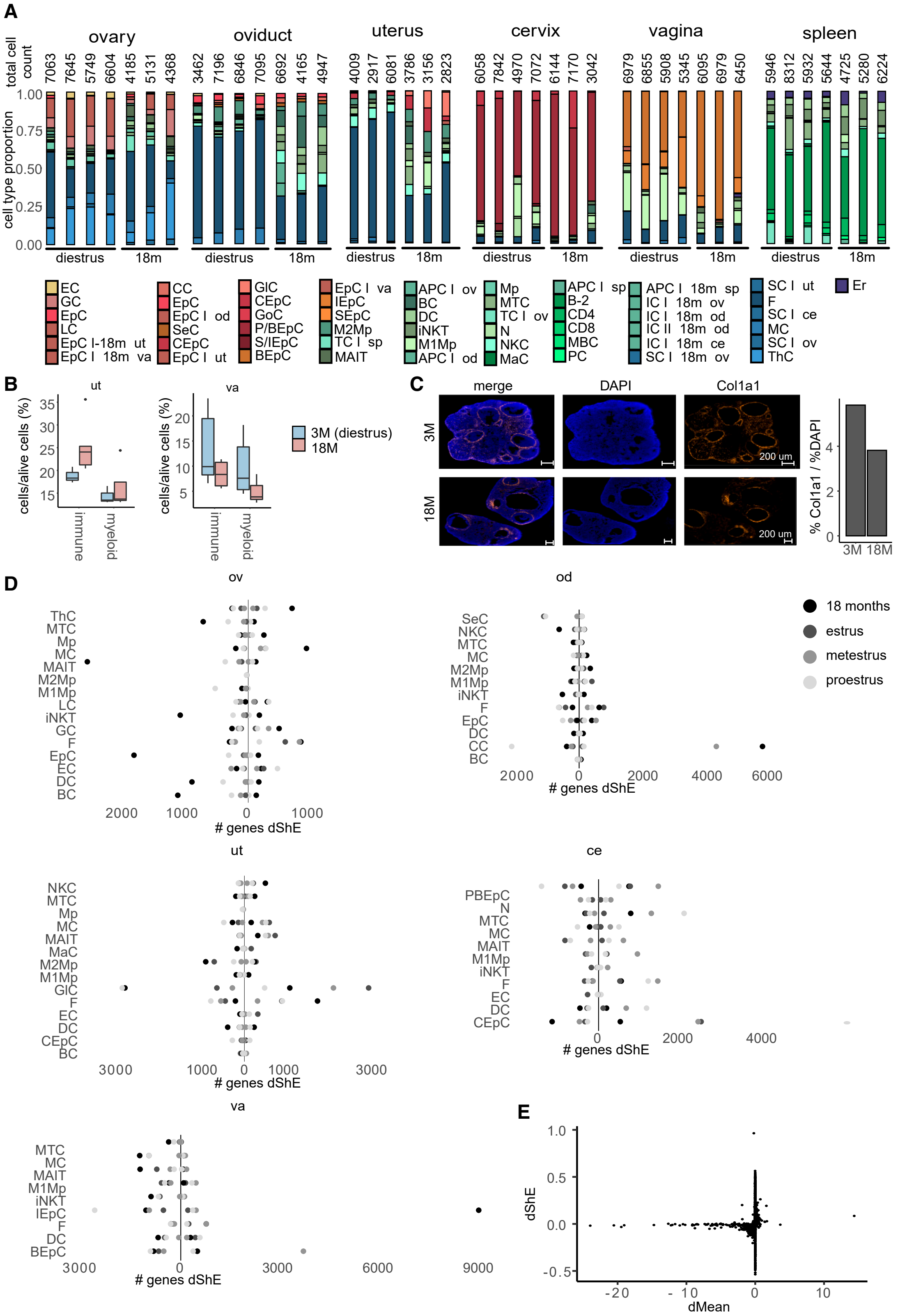

(legend on next page)

**Figure S8. Single-cell characterization of the aged FRT, related to Figure 5**

(A) Barplots showing the % of each cell type in the ovary, oviduct, uterus, cervix, vagina, and spleen in old age and diestrus in each biological replicate.

(B) Quantification of immune and myeloid cell proportions in the uterus and vagina of young and old mice using FACS. Uterus: young n = 3; old n = 5. Vagina: young n = 6; old n = 5.

(C) Expression of Col1a1 in the uterus of young and old mice, detected using RNA hybridization. Col1a1 signal is defined as % area of total DAPI area. Bar height indicates the average value of two biological replicates.

(D) Number of genes with differential Shannon entropy (ShE) of all cell types in the ovary, oviduct, uterus, cervix, and vagina in diestrus compared with other phases of the cycle and old age. Dots on the left side of the y axis indicate increased entropy relative to diestrus (e.g., higher ShE in old age compared with diestrus) and dots on the right side indicate decreased entropy.

(E) Difference of mean plotted against differential Shannon entropy between young and old for all genes in fibroblasts in the ovary.